CAM evolution is associated with gene family expansion in an explosive bromeliad radiation

Short title: CAM is associated with gene family expansion

Clara Groot Crego[1,2], Jaqueline Hess[1,3], Gil Yardeni[1,4], Marylaure de La Harpe[1,5], Clara Priemer[6], Francesca Beclin[1,2,7], Sarah Saadain[1,2], Luiz A. Cauz-Santos[1], Eva M. Temsch[1], Hanna Weiss-Schneeweiss[1], Michael H.J. Barfuss[1], Walter Till[1], Wolfram Weckwerth[6,8], Karolina Heyduk[9], Christian Lexer[1,†], Ovidiu Paun[1]*, Thibault Leroy[1,10]*

[1]Department of Botany and Biodiversity Research, University of Vienna, Vienna, Austria
[2]Vienna Graduate School of Population Genetics, Vienna, Austria
[3]Cambrium GmbH, Max-Urich-Str. 3, 13055 Berlin, Germany
[4]Institute of Computational Biology, Department of Biotechnology, University of Life Sciences and Natural Resources (BOKU), Muthgasse 18, 1190 Vienna, Austria.
[5]Office for Nature and Environment, Canton of Grisons, Chur, Switzerland
[6]Department of Functional and Evolutionary Ecology, Molecular Systems Biology (MOSYS), University of Vienna, Vienna, Austria
[7]Gregor Mendel Institute, Austrian Academy of Sciences, Vienna BioCenter, Vienna, Austria
[8]Vienna Metabolomics Center (VIME), University of Vienna, Vienna, Austria
[9]Ecology and Evolutionary Biology, University of Connecticut, Storrs, CT USA
[10]GenPhySE, Université de Toulouse, INRAE, ENVT, Castanet Tolosan, France

[†]deceased
*Joint last authors

Correspondence to: clara.groot.crego@univie.ac.at, ORCID: 0000-0002-4547-3608

The author(s) responsible for distribution of materials integral to the findings presented in this article in accordance with the policy described in the Instructions for Authors (https://academic.oup.com/plcell/pages/General-Instructions) is (are): Clara Groot Crego (clara.groot.crego@univie.ac.at).

1. Abstract

The subgenus *Tillandsia* (Bromeliaceae) belongs to one of the fastest radiating clades in the plant kingdom and is characterised by the repeated evolution of Crassulacean Acid Metabolism (CAM). Despite its complex genetic basis, this water-conserving trait has evolved independently across many plant families and is regarded as a key innovation trait and driver of ecological diversification in Bromeliaceae. By producing high-quality genome assemblies of a *Tillandsia* species pair displaying divergent photosynthetic phenotypes, and combining genome-wide investigations of synteny, TE dynamics, sequence evolution, gene family evolution and temporal differential expression, we were able to pinpoint the genomic drivers of CAM evolution in *Tillandsia*. Several large-scale rearrangements associated with karyotype changes between the two genomes and a highly dynamic TE landscape shaped the genomes of *Tillandsia*. However, our analyses show that rewiring of photosynthetic metabolism is mainly obtained through regulatory evolution rather than coding sequence evolution, as CAM-related genes are differentially expressed across a 24-hour cycle between the two species, but are no candidates of positive selection. Gene orthology analyses reveal that CAM-related gene families manifesting differential expression underwent accelerated gene family expansion in the constitutive CAM species, further supporting the view of gene family evolution as a driver of CAM evolution.

Word count for Abstract: **200**

Word count for Introduction: **1,154**

Word count for Results: **4,121**

Word count for Discussion: **1,590**

Total word count: 7,065

2. Introduction

Crassulacean Acid Metabolism (CAM) is a photosynthetic phenotype playing a major role in plant adaptation to arid environments and the epiphytic lifeform (Winter and Smith, 2012; Cushman, 2001; Silvera et al., 2010), and has been described as a key innovation trait driving plant diversification and speciation in several plant lineages (Quezada and Gianoli, 2011; Silvera et al., 2009; Ogburn and Edwards, 2009). CAM functions as a carbon concentrating mechanism by assimilating CO_2 overnight and storing it as malate in the vacuole, which greatly enhances the efficiency of Rubisco, the first enzyme of the Calvin cycle (Osmond, 1978). This also has the secondary effect of improving the plant's overall water use efficiency by reducing evapotranspiration, as stomata can remain closed during the day (Borland et al., 2014). Though often presented as a discrete trait, CAM actually encompasses a large spectrum of photosynthetic phenotypes including intermediate and facultative forms (Edwards, 2023). Phenotypes from this CAM continuum have evolved repeatedly in at least 37 plant families (Winter et al., 2021), yet the underlying evolutionary mechanisms allowing this complex and diverse trait to emerge multiple times throughout plant history are not fully understood.

Due to the sparse availability of CAM plant genomes, most studies on CAM evolution have focussed on transcription levels and sequence evolution to understand its underlying genetic drivers. However, novel variation can be generated by other mechanisms which have not been investigated thoroughly in the context of CAM evolution. For example, several studies have suggested a potential importance of gene family expansion as a driver of CAM evolution (Cai et al., 2015; Silvera et al., 2014). In C4 plants, duplicated gene copies tend to be more often retained compared to closely related C3 lineages (Hoang et al., 2023). Gene duplication occurs at higher rates than point mutation in many lineages (Katju and Bergthorsson, 2013) and can lead to novel functional variation through dosage effects, neo-functionalization, or subfunctionalization (Ohno, 1970), as observed in teleost fish (Arnegard et al., 2010; Moriyama et al., 2016) and orchids (Mondragón-Palomino and Theissen, 2009). Another form of structural variation that can contribute to the evolution of complex traits is TE insertion in and around genes, which has been shown to play a role in local adaptation, for example in *Arabidopsis* (Baduel et al., 2019). Finally, large-scale rearrangements such as chromosomal fusions, inversions or translocations can increase linkage between co-adapted alleles and generate reproductive barriers (Luo et al., 2018; Lowry and Willis, 2010).

91 The adaptive radiation of *Tillandsia* subgenus *Tillandsia* (Bromeliaceae) is part of one of
92 the fastest diversifying clades known in the plant kingdom (Tillandsioideae) (Givnish et al., 2014)
93 and is characterised by a number of key innovation traits such as the epiphytic lifestyle, absorptive
94 trichomes, water-impounding tanks and photosynthetic metabolism driving extraordinary diversity
95 both on the taxonomic and ecological level (Barfuss et al., 2016). The group displays a broad range
96 of phenotypes of the CAM continuum, resulting from repeated evolution of constitutive CAM
97 (Crayn et al., 2015; De La Harpe et al., 2020). CAM evolution has been described as an ecological
98 driver of diversification in the subgenus *Tillandsia* (Barfuss et al., 2016; Crayn et al., 2004), and
99 across Bromeliaceae in general (Givnish et al., 2014; Crayn et al., 2004; Benzing and Bennett,
100 2000). This renders the radiation a fascinating system both for studies on speciation and rapid
101 adaptation generally, and for studies on CAM evolution specifically, as comparative investigations
102 between recently diverged species with contrasting phenotypes prevent the overestimation of
103 evolutionary changes needed to evolve adaptations such as CAM (Heyduk et al., 2019a).
104 While Bromeliaceae is generally regarded as a homoploid radiation with conserved
105 chromosome counts and little genome size variation (Gitaí et al., 2014), more recent work has
106 pointed at a high "genomic potential" of the subgenus *Tillandsia*, notably from elevated gene loss
107 and duplication rates (De La Harpe et al., 2020), providing an exemplary system to study the role
108 of genome evolution and structural variation in CAM evolution. Not only are adaptive radiations
109 like *Tillandsia* characterised by repeated evolution of key innovation traits, the short timescales at
110 which novel variation arises in these systems challenge classical views of adaptive evolution,
111 stimulating a range of studies pointing at the potential importance of genome evolution as a
112 genomic driver of diversification (McGee et al., 2020; Brawand et al., 2015; Cicconardi et al.,
113 2021).
114 In this study, we comparatively investigated *de novo* assembled genomes of two
115 ecologically divergent members of the subgenus *Tillandsia* to further our understanding of genome
116 evolution in this recent radiation and its link to CAM evolution as a key innovation trait. *Tillandsia*
117 *fasciculata* (Fig. 1a) displays a set of phenotypes typically described as "grey" or "atmospheric"
118 *Tillandsia* (Benzing and Bennett, 2000): a dense layer of absorptive, umbrella-shaped trichomes,
119 CAM photosynthesis and occurrence in arid places with high solar incidence and low rainfall. On
120 the other hand, *T. leiboldiana* (Fig. 1b) represents a typical "green" *Tillandsia* displaying tank
121 formation, C3-like leaf morphology, a sparse layer of absorptive trichomes and occurrences in

cooler, wetter regions. While not sister species, *T. fasciculata* and *T. leiboldiana* belong to sister clades displaying a shift in photosynthetic metabolism (Fig. 1c), and represent phenotypic extremes within subgenus *Tillandsia*. Their photosynthetic metabolisms have been described as strong CAM for *T. fasciculata,* and C3 for *T. leiboldiana* based on carbon isotope ratios ($\delta^{13}C_{T.fasciculata}$ = -11.9 / -16.1; $\delta^{13}C_{T.leiboldiana}$ = -28.0 / -31.3) reported by Crayn et al., (2015) and De La Harpe et al., (2020) respectively. These are some of the most distinct values reported for the subgenus.

However, due to the limited ability of carbon isotope measurements in capturing intermediate CAM phenotypes and therefore representing the full CAM continuum (Messerschmid et al., 2021; Pierce et al., 2002), the exact photosynthetic phenotypes of *T. leiboldiana* and *T. fasciculata* need to be corroborated to fully understand what range of the CAM continuum is truly encompassed in the subgenus. By characterising the photosynthetic metabolisms of *T. leiboldiana* and *T. fasciculata* and investigating genomic variation between these two species on multiple levels, from karyotype, chromosomal rearrangements, to molecular evolution, gene family evolution and temporal differential gene expression, we thoroughly explore the degree of genomic divergence found within this radiation and the link between this variation and the evolution of a key innovation trait. We ascertain that the photosynthetic metabolisms of these species are clearly distinct, with *T. fasciculata* at the late stages of CAM evolution (i.e., constitutive, strong CAM), and *T. leiboldiana* likely at the very early stages (i.e., no night-time malate accumulation, but CAM-like expression profiles of certain enzymes). We further document karyotype differences, multiple chromosomal rearrangements, distinct TE landscapes and gene family evolution rates between the two species. We find evidence that molecular variation underlying the difference in phenotype is largely found at the transcriptomic level. We also find a clear association between CAM-related temporal gene expression differences and both gene family expansion in the constitutive CAM plant and pre-existing gene duplications shared between both species.

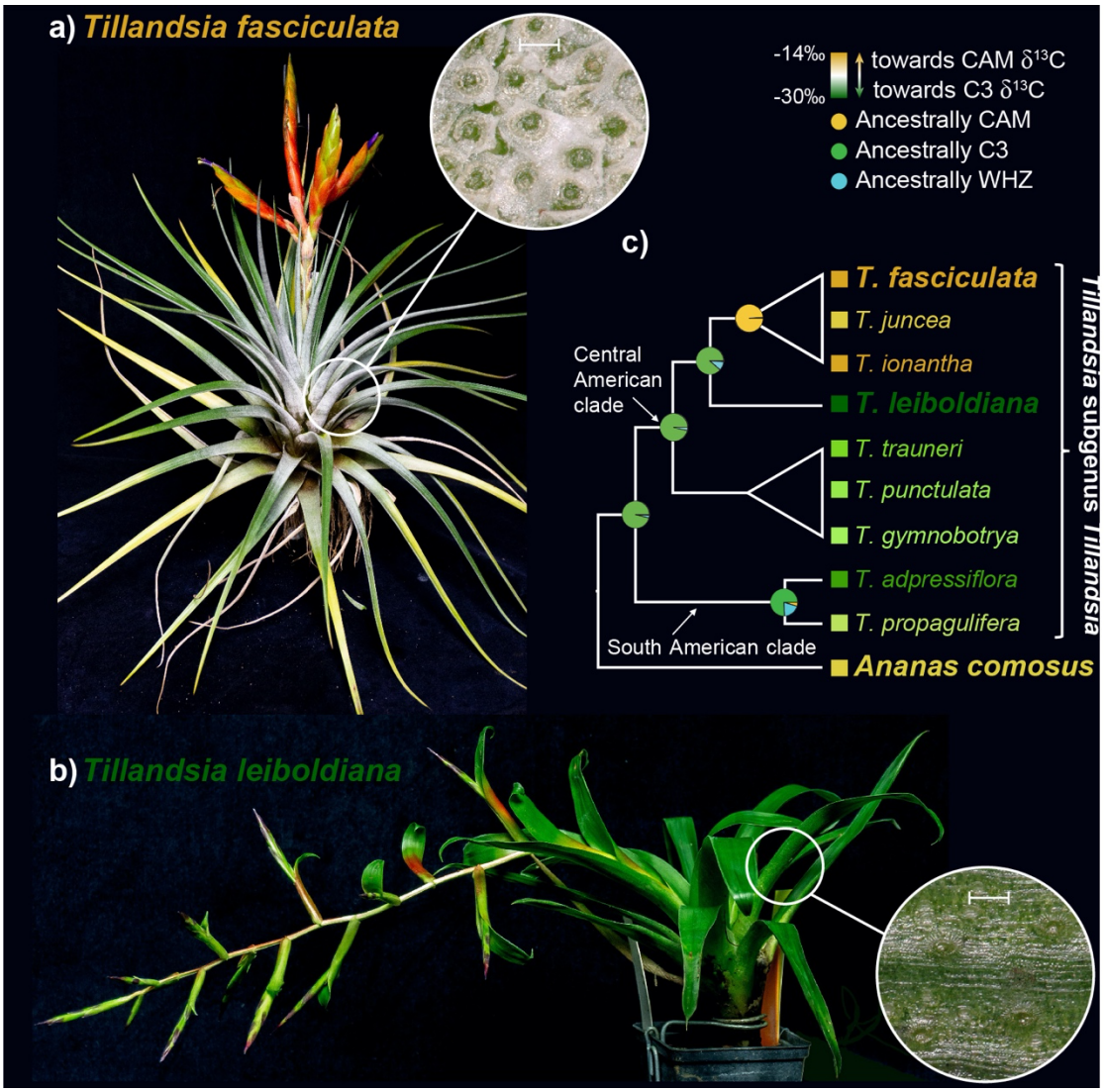

Figure 1: a) Tillandsia fasciculata*, a "grey" or "atmospheric"* Tillandsia *with a dense layer of umbrella-shaped trichomes (inset), carbon isotope values within the CAM range, a lack of water-impounding tank and roots adapted to the epiphytic lifestyle. The leaf close-up is at a 100 µm scale (also in b).* ***b)*** Tillandsia leiboldiana*, a green* Tillandsia *with C3-like leaf morphology and carbon isotope values, an impounding tank and a sparse trichome layer (inset).* ***c)*** *Schematic representation of the evolutionary relationship between the two investigated species of* Tillandsia *within the subgenus. Colours indicate reported carbon isotope values* (De La Harpe et al., 2020; Crayn et al., 2015)*. The average was taken when multiple values have been reported for the same species. Pie charts at internal nodes show the ancestral state of photosynthetic metabolism as reported in De La Harpe et al. 2020. WHZ stands for Winter-Holtum Zone* (Males, 2018) *and represents intermediate forms of the CAM continuum.*

3. Results

3.1. Photosynthetic phenotypes of *T. fasciculata* and *T. leiboldiana*

To better understand the difference in photosynthetic metabolism between *T. fasciculata* and *T. leiboldiana*, we measured metabolite abundances with GC-MS for six samples per species at six timepoints across a 24-hour cycle. The overall composition of 49 metabolite abundances separate samples of both species within the first two principal components (Fig. 2a), which combined explain 41.5 % of variance. This suggests a pronounced general metabolic differentiation between *T. fasciculata* and *T. leiboldiana*. Besides amino acids, the organic acids malate, citrate and gluconic acid contribute most to this differentiation along PC1 (Fig. S1), which is a common pattern for species with diverging photosynthetic metabolism (De La Harpe et al., 2020; Benzing and Bennett, 2000; Popp et al., 2003). Sugars appear large contributors to differentiation along PC2 (Fig. S1).

Overnight malate accumulation is a core feature of CAM photosynthesis and therefore an indicator of the respective photosynthetic phenotypes of *T. fasciculata* and *T. leiboldiana*. Malate abundances in the leaf fluctuated strongly in *T. fasciculata* over 24 hours, with highest median abundances around midday (D+5) and lowest abundances in the early night (N+1), representing a 3.8-fold difference (Fig. 2b). In comparison, malate abundances were overall lower for *T. leiboldiana* and fluctuated less. The highest median abundance in the latter species was found at N+1, while the lowest was found at D+5, representing a 2.2-fold difference. Interestingly, the accumulation times of malate seem reversed in the two species, with the highest abundances in *T. fasciculata* found at the time of lowest abundances in *T. leiboldiana* and vice versa. The reversed timing of malate accumulation has been described as a key difference between C3 and CAM metabolisms ((Winter and Smith, 2022), but see also (Bräutigam et al., 2017)). The median accumulation in malate within 24-hours differs significantly between, with a 3.2-fold higher value in *T. fasciculata* than in *T. leiboldiana* (Wilcoxon rank-sum test p-value = 8.6E-03, Fig. 2c).

Overall, the malate accumulation curves suggest distinct photosynthetic phenotypes for *T. fasciculata* and *T. leiboldiana*. *T. fasciculata* appears to behave as a constitutive CAM plant in standard conditions, accumulating malate from the early night until the early day, while *T. leiboldiana*'s flux is more C3-like, without a clear accumulation overnight.

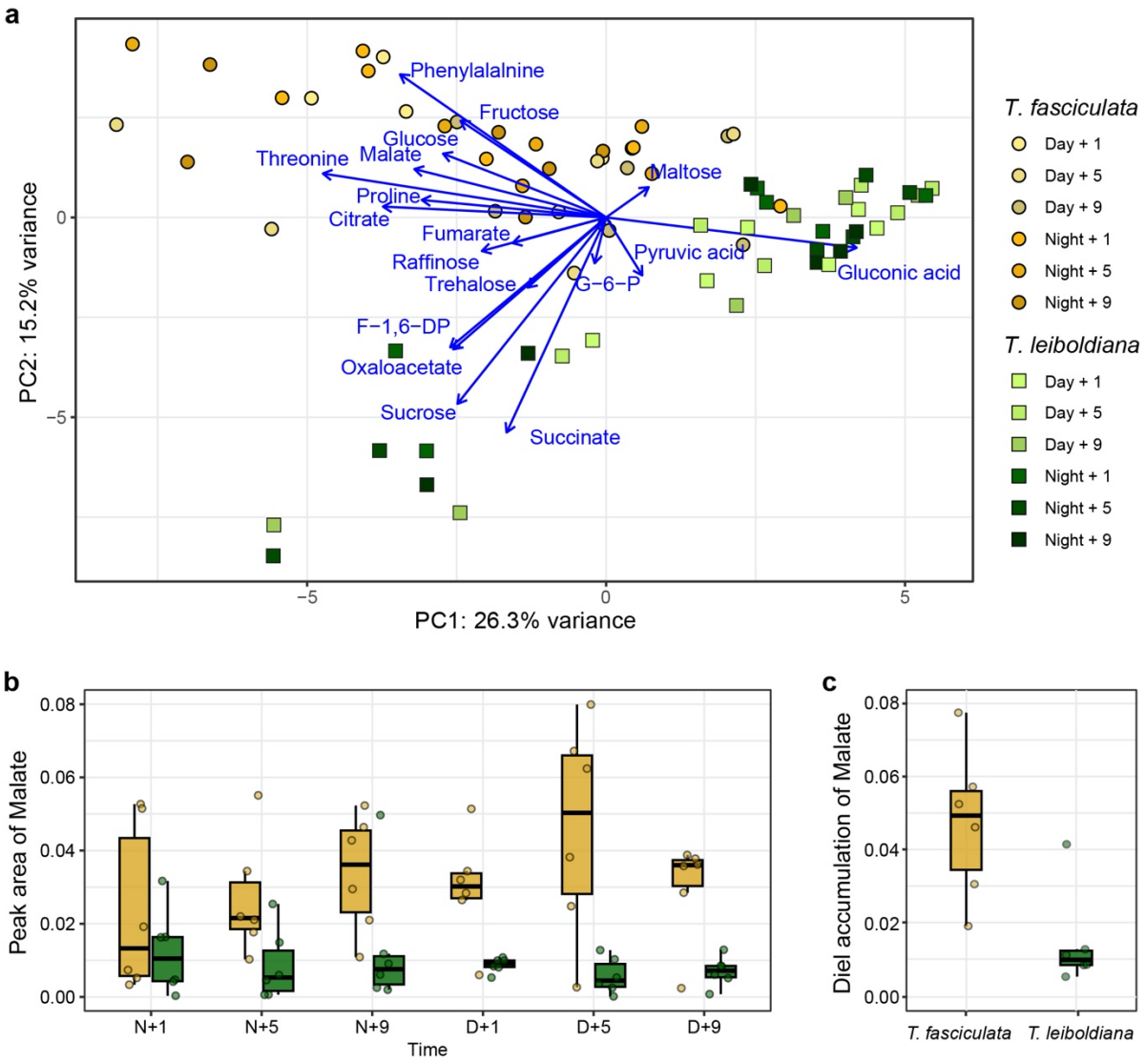

***Figure 2**: Metabolomic analyses of* T. fasciculata *and* T. leiboldiana *leaf material throughout a 24-hour cycle. Abundances of individual metabolites were measured with GC-MS and normalised against the Main Total Ion Count (MTIC). **a)** Principal component analysis of metabolic composition of 72 leaf samples based on 77 metabolic compounds including soluble sugars, amino acids, and organic acids. The first and second principal components are displayed. Blue arrows show the loadings of a subset of metabolites relevant for photosynthetic metabolism. **b)** Malate abundance in leaf material of* T. fasciculata *and* T. leiboldiana *at six timepoints across a 24-hour cycle. Dots represent individual observations across timepoints. Timepoints are noted as hours into the day (D) or into the night (N). **c)** Distribution of per-individual accumulation of malate per species over a 24-hour cycle. Accumulations were obtained by taking the difference in malate abundance between the highest and lowest reported abundances across time for each accession.*

201 **3.2. Genome assembly and annotation**

202 We constructed *de novo* haploid genome assemblies for both species (Table S1) using a
203 combination of long-read (PacBio), short read (Illumina) and chromosome conformation capture
204 (Hi-C) data. This resulted in assemblies of 838 Mb and 1,198 Mb with an N50 of 23.6 and 43.3
205 Mb in *T. fasciculata* and *T. leiboldiana* respectively. The assembly sizes closely match the
206 estimated genome size of each species based on flow cytometry and k-mer analysis (Table S2, SI
207 Notes 1-2). The 25 and respectively 26 longest scaffolds (hereafter referred to as 'main scaffolds')
208 contain 72 % and 75.5 % of the full assembly, after which scaffold sizes steeply decline (SI Note
209 3, Fig. S2). The number of main scaffolds corresponds with the species karyotype in *T. fasciculata*,
210 but deviates from the *T. leiboldiana* karyotype (SI Note 1), suggesting that a few fragmented
211 chromosome sequences remain in the latter assembly.

212 Structural gene annotation resulted in a total of 34,886 and 38,180 gene models in *T.*
213 *fasciculata* and *T. leiboldiana* respectively, of which 92.6 % and 71.9 % are considered robust
214 based on additional curation (Methods, Section 5). Annotation completeness was evaluated with
215 BUSCO using the Liliopsida dataset resulting in a score of 89.7 % complete genes in *T. fasciculata*
216 and 85.3 % in *T. leiboldiana* (Table S2).

217

218 **3.3. Genic, repetitive and GC content**

219 TE annotation performed with EDTA (Ou et al., 2019) revealed a total repetitive content
220 of 65.5 % and 77.1 % in *T. fasciculata* and *T. leiboldiana* respectively. This closely matches
221 estimates derived from k-mer analyses (66 % and 75 %, SI Note 2). Compared to *T. fasciculata*,
222 the repetitive content in *T. leiboldiana* is enriched for Gypsy LTR retrotransposon and *Mutator*
223 DNA transposon content, with a 1.7-fold and 4.2-fold increase in total covered genomic length,
224 respectively (Table S3).

225 Repetitive content per scaffold is negatively correlated with gene count in both assemblies
226 (Kendall's correlation coefficient: -0.79 in *T. fasciculata*, -0.82 in *T. leiboldiana,* p-values < 2.2E-
227 16), with gene-rich regions in distal positions (Fig. 3a, green track) and repetitive regions primarily
228 in median positions (Fig. 3a, yellow track). This pattern is accentuated in *T. leiboldiana*: on
229 average, the repetitive-to-exonic content per scaffold is 1.6 times larger compared to *T. fasciculata*
230 (Mann Whitney U, p-value = 4.3E-04). The genome size difference between the two assemblies is

therefore mostly explained by differential accumulation of TE content, mostly in heterochromatic regions.

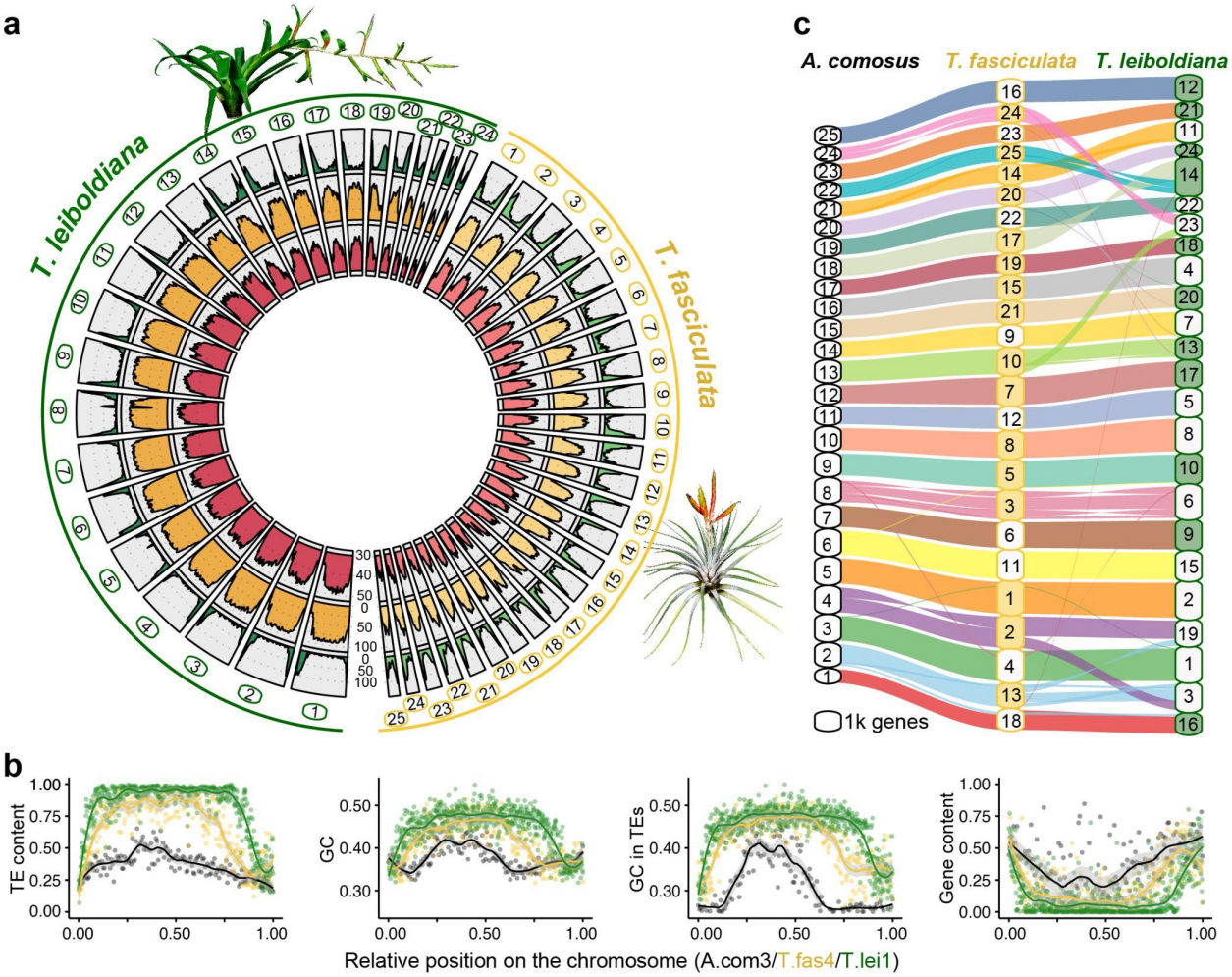

Figure 3: a) *Circular overview of the main scaffolds of the* T. fasciculata *(right) and* T. leiboldiana *(left) genome assemblies. Scaffolds 25 and 26 of* T. leiboldiana *are not shown due to their reduced size. Going inwards, the tracks show: (1, green) gene count; (2, yellow) proportion of repetitive content; (3, red), and GC content per 1-Mb windows.* ***b)*** *TE and GC content, GC content exclusively in TEs, and genic content in a triplet of syntenic scaffolds between* Ananas comosus *(LG3, black),* T. fasciculata *(scaffold 4, grey) and* T. leiboldiana *(scaffold 1, green; see Fig. S3 for other syntenic chromosomes).* ***c)*** *Syntenic plot linking blocks of orthologous genes between* A. comosus*,* T. fasciculata *and* T. leiboldiana*. The size of each scaffold on the y-axis is proportional to genic content and therefore does not represent the true scaffold size. Colour-filled boxes indicate scaffolds with reversed coordinates as compared to the sequences in* A. comosus*.*

GC content is negatively correlated with gene content in both species (Kendall's correlation coefficient: -0.68 in *T. fasciculata*, -0.71 in *T. leiboldiana,* p-values < 2.2E-16, red track in Fig. 3a, detailed in Fig. 3b). By visualising GC and TE content across a syntenic chromosome triplet of *A. comosus*, *T. fasciculata* and *T. leiboldiana,* we show that this relationship can be mostly explained by elevated GC content in repetitive regions (Fig. 3b). TE-rich regions indeed exhibit a much higher GC content than TE-poor regions, a pattern which is exacerbated as the overall TE content per species increases (Fig. 3b, SI Note 4).

3.4. Synteny and chromosomal evolution

Cytogenetic karyotyping (SI Note 1) revealed a difference of six chromosome pairs between *T. fasciculata* (2*n* = 50) and *T. leiboldiana* (2*n* = 38), which is atypical in this largely homoploid clade with generally constant karyotype (Gitaí et al., 2014; Brown and Gilmartin, 1989). To investigate orthology and synteny, we inferred orthogroups between protein sequences of *Ananas comosus* (Ming et al., 2015) (pineapple), *T. fasciculata* and *T. leiboldiana* using Orthofinder (Emms and Kelly, 2019). This resulted in 21,045 (78 %), 26,325 (87.5 %) and 23,584 (75 %) gene models assigned to orthogroups respectively, of which 10,021 were single-copy orthologs between all three species (Table S4).

Syntenic blocks were then defined across all three assemblies using Genespace (Lovell et al., 2022) (Fig. 3c). Remarkably, the three-way synteny analysis between *A. comosus, T. fasciculata* and *T. leiboldiana* show higher synteny between *T. fasciculata* and *A. comosus* than between the two *Tillandsia* genomes, which could be explained by *T. leiboldiana'*s diverged karyotype. While the difference in karyotype could have arisen from chromosomal loss in *T. leiboldiana*, our Genespace analysis reveals conserved synteny between the two *Tillandsia* assemblies without major orphan regions in *T. leiboldiana*. This is consistent with a scenario of chromosomal fusion, rather than loss. We found clear evidence of such a fusion on scaffold 14 in *T. leiboldiana* (Fig. 3c, Fig. S4a), which was confirmed with in-depth analyses of potential breakpoints (SI Note 5). However, chromosomal rearrangements are not limited to fusions, since we also detected two major reciprocal translocations (Fig. 3c, hereafter referred as Translocations 1 and 2, Fig. S4b-c).

274 **3.5. Gene family evolution**

275 6,261 genes in *T. fasciculata* and 4,693 genes in *T. leiboldiana* were assigned to non-unique
276 gene families with multiple gene copies in at least one species, after correcting gene family sizes
277 (Table S4). On average, the multicopy gene family size is 1.3x larger in *T. fasciculata* than in *T.*
278 *leiboldiana* (Mann Whitney U, p-value: 8.8E-16, Fig. 4a).

279 To investigate the role of expanded gene families in CAM evolution, we combined gene
280 ontology (GO) enrichment tests on multicopy orthogroups (SI Note 6) with a targeted search of
281 known genes involved in the CAM pathway. This highlighted 25 multi-copy gene families with
282 functions putatively related to CAM (Table S5), of which 17 have expanded in *T. fasciculata* and
283 eight in *T. leiboldiana.* Families expanded in *T. fasciculata* included a malate dehydrogenase
284 (MDH) and a β-carbonic anhydrase (CA), which are putatively involved in the carbon fixation
285 module of CAM photosynthesis, and subunits of the two vacuolar pumps (V-ATPase and V-
286 PPiase) known to energise the night-time transport of malate in pineapple (McRae et al., 2002)
287 (Table S5). Additionally, two enolase families (members of the glycolysis pathway), a vacuolar
288 acid invertase putatively involved in day-time soluble sugar accumulation in the vacuole (McRae
289 et al., 2002; Holtum et al., 2005), and a pyrophosphate-dependent phosphofructokinase associated
290 with night-time conversion of soluble sugars through the glycolysis to PEP (Carnal and Black,
291 1989) were expanded in *T. fasciculata*. Two subunits of succinate dehydrogenase, a member of
292 the tricarboxylic acid cycle and the electron transport chain which also plays a role in stomatal
293 opening regulation, a relevant aspect of CAM photosynthesis (Araújo et al., 2011), were also
294 expanded in *T. fasciculata*. XAP5 CIRCADIAN TIMEKEEPER (XCT), a regulator of circadian
295 rhythm and disease resistance (Liu et al., 2022) which was previously identified as undergoing
296 rapid gene family evolution in *Tillandsia* (De La Harpe et al., 2020) is also expanded in *T.*
297 *fasciculata*.

298 Gene families expanded in *T. leiboldiana* contained three members of the glycolysis, two
299 aquaporins, a member of the tricarboxylic acid cycle and a regulator of stomatal opening (Table
300 S5).

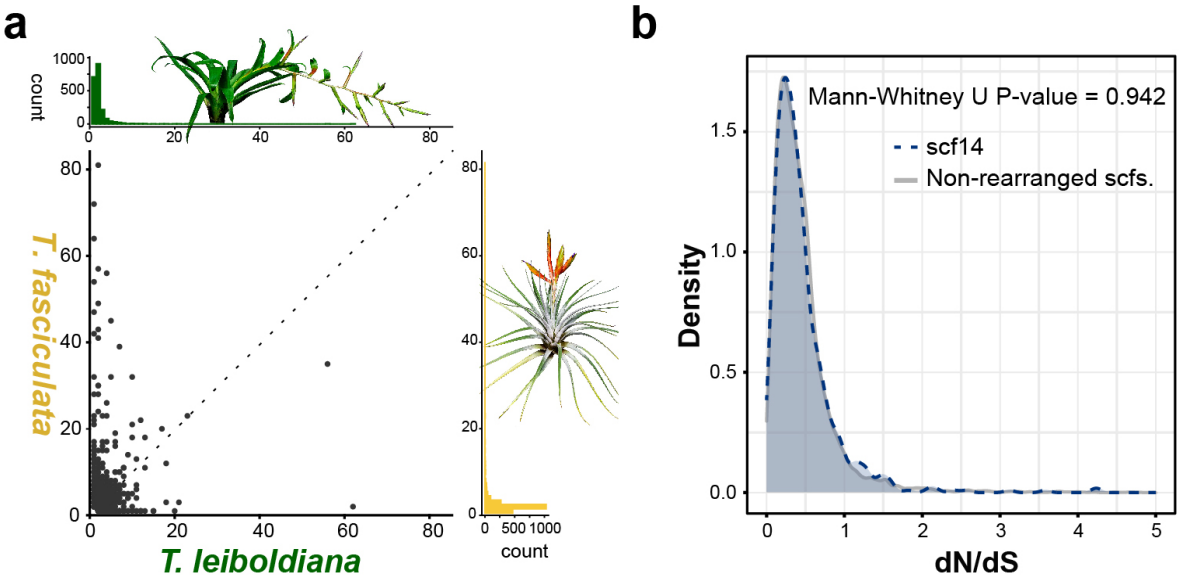

c

Orthogroup	dN/dS	adj-P	Function
OG0002972	∞	0.00162	jacalin-related lectin 3-like
OG0005000	∞	0.00628	cucumber peeling cupredoxin-like
OG0006253	∞	0.00066	mitochondrial prohibitin-3
OG0009278	∞	0.00155	chloroplastic Peroxiredoxin-2E-2
OG0012770	∞	0.01374	metallo-hydrolase/oxidoreductase superfamily protein
OG0011786	9.3	0.00008	U-box_domain-containing_protein
OG0015603	8.1	0.01575	anaphase-promoting complex subunit CDC27
OG0009004	3.1	0.01148	Hydroquinone glycosyltransferase
OG0008977	2.6	0.00512	glutamate receptor 2.8-like
OG0010014	2.0	0.00603	Glycerophosphodiester phosphodiesterase GDPDL7

Figure 4: a) *Scatterplot: composition of per-species gene counts among orthogroups. Upper histogram: distribution of per-orthogroup gene count in* T. fasciculata*. Lower histogram: distribution of per-orthogroup gene count in* T. leiboldiana*.* ***b)*** *Distribution of* d_N/d_S *values of one-to-one orthologs across non-rearranged scaffolds (grey profile) and scaffold 14 in* T. leiboldiana *(blue profile), which is the result of a fusion.* ***c)*** *Single-copy orthogroups with significant* d_N/d_S *values and their functions. Three uncharacterized genes that are excluded here are detailed in Table S6. Infinite* d_N/d_S *values correspond to genes with* $d_S=0$ *(no synonymous substitutions), an expected situation considering the low divergence of the two species. Further explanation about the biological significance of these functions can be found in SI Note 7.*

312 **3.6. Adaptive sequence evolution**

313 Adaptive sequence evolution was evaluated in 9,077 one-to-one orthologous gene pairs
314 using the non-synonymous to synonymous substitution ratio ($\omega = d_N/d_S$). Little among-scaffold
315 variation in d_N/d_S was observed, with per-scaffold median d_N/d_S values ranging from 0.32 to 0.39
316 in *T. fasciculata* and 0.31 to 0.4 in *T. leiboldiana* (Fig. S5a). Regions of large chromosomal
317 rearrangement such as the fused scaffold 14 in *T. leiboldiana* do not exhibit strong signatures of
318 fast coding sequence evolution (Fig. 4b), though for Translocation 1, d_N/d_S values are slightly, yet
319 significantly, lower for scaffold 13 in *T. fasciculata* and scaffold 19 in *T. leiboldiana* (Fig. S5b, SI
320 Note 5).

321 Among the 9,077 orthologous gene pairs, 13 candidates (0.21%) exhibit a significant d_N/d_S
322 > 1 (adjusted p-value < 0.05, Fig. 4c, Table S6, SI Note 7). Notably, we recover a significant signal
323 in a type B glycerophosphodiester phosphodiesterase (GDPDL-7). GDPDL's are involved in cell
324 wall cellulose accumulation and pectin linking, and play a role in trichome development (Hayashi
325 et al., 2008), a main trait differentiating the two species and more broadly, green and grey
326 *Tillandsia*. Additionally, GDPDL-7 may be involved in response to drought and salt stress (Cheng
327 et al., 2011).

328 A glutamate receptor (GLR) 2.8-like also exhibits a significant $d_N/d_S > 1$. By mediating
329 Ca^{2+} fluxes, GLRs act as signalling proteins and mediate a number of physiological and
330 developmental processes in plants (Weiland et al., 2015), including stomatal movement (Kong et
331 al., 2016). Although it is associated with drought-stress response in *Medicago trunculata* (Philippe
332 et al., 2019), the specific function of GLR2.8 still remains unknown.

333

334 **3.7. Gene expression analyses**

335 To study gene expression differences linked to distinct photosynthetic phenotypes, we
336 performed a time-series RNA-seq experiment using six plants of each species (Table S1, SI Note
337 8), sampled every four hours in a 24-hour period. We recovered 907 genes with a differential
338 temporal expression (DE) profile between *T. fasciculata* and *T. leiboldiana*. Among them are 46
339 known CAM-related genes and 22 genes associated with starch metabolism and
340 glycolysis/gluconeogenesis (Fig. S6). GO term enrichment of the 907 DE genes revealed many
341 CAM-related functions such as malate and oxaloacetate transport, circadian rhythm, light
342 response, water and proton pumps, sucrose and maltose transport and starch metabolism (Table

343 S7; Fig. 5a). While none of the candidate genes for adaptive sequence evolution recovered in this
344 study were differentially expressed, nine of 22 genes reported by De La Harpe et al. 2020 as
345 candidates for adaptive sequence evolution during transitions to constitutive CAM in the wider
346 context of the genus *Tillandsia* were also differentially expressed in this study (Table S7).

347 Core CAM enzymes phosphoenolpyruvate carboxylase (PEPC) and phosphoenolpyruvate
348 carboxylase kinase (PEPC kinase, PPCK) display clear temporal expression cycling in *T.*
349 *fasciculata* (Fig. 5c, S5). PPCK also shows a night-time increase in expression in *T. leiboldiana*
350 (Fig. S7), albeit with a milder temporal effect, a phenomenon that has been documented before in
351 C3-assigned *Tillandsia* (De La Harpe et al., 2020) and also in other C3-like species belonging to
352 CAM- and C4-evolving lineages (Heyduk et al., 2019b, 2019a). Clustering analysis distributed DE
353 genes across seven clusters with sizes ranging from 209 to 38 genes (Table S7). CAM-related
354 genes were distributed across six of seven clusters, highlighting the diversity of expression profiles
355 associated with CAM (Fig. S8). While core CAM genes (see Fig. 6) are mainly found in cluster 5,
356 we find malate transporters in cluster 1, circadian regulators in clusters 2 and 3, sugar transport in
357 clusters 3 and 6, and vacuolar transport regulators in clusters 2, 4 and 6. Cluster 7, though not
358 containing any core CAM candidate genes, was enriched for salt and heat stress response and
359 contains a mitochondrial isocitrate dehydrogenase, which has been proposed as an alternative
360 carbon fixator in CAM plants (Tay et al., 2021; Töpfer et al., 2020).

361 The expression curves of the respective clusters (Fig. S8) demonstrate a complex web of
362 expression changes between photosynthetic phenotypes. The most common expression change
363 pattern among CAM-related genes is an overall increase in expression in the strong CAM plant
364 (*T. fasciculata*), paired with increased diel cycling peaking in the early night (clusters 2, 5 and 6).
365 This involved members of the night-time carbon fixating module of CAM such as PEPCK, PPCK
366 and MDH, enzymes involved in malate transport as V-ATPase and several glycolysis enzymes
367 such as glucose-6-phosphate isomerase, aldolase, Ppi-dependent phosphofructokinase (PFK) and
368 enolase (Fig. 6, S6). Enzymes of both soluble sugar transport (SUT2, ERD6, cluster 6) and starch
369 metabolism (Starch synthase I, α- and β-amylase and glucose-6-phosphate/phosphate translocator
370 (GPT), cluster 5 and 6) are overall up-regulated and show cycling expression curves in *T.*
371 *fasciculata* compared to *T. leiboldiana,* all showing highest activity in the late day. While the
372 increased night-time expression of Ppi-dependent PFK suggests a primary role of soluble sugars
373 as night-time source for PEP (Carnal and Black, 1989) in CAM *Tillandsia*, the simultaneously

374 cycling expression patterns in starch metabolic enzymes point also at transitory starch as a
375 potential source. A handful of CAM-related genes show increased expression in *T. leiboldiana*:
376 aluminium-activated malate transporter (ALMT), secondary vacuolar proton pump AVP1, which
377 also displays a phase shift peaking later in the night in *T. fasciculata*, and three circadian clock
378 regulators (LHY, GI and RVE1, cluster 1), which all show similar but reduced cycling patterns in
379 *T. fasciculata* compared to *T. leiboldiana*. We also see a phase shift in succinate dehydrogenase
380 peaking earlier in the night in *T fasciculata* versus *T. leiboldiana*'s early morning peak.

381 Overall, most CAM-related DE gene expression profiles align with the view that *T.*
382 *fasciculata* is a constitutive CAM plant while *T. leiboldiana* performs a C3-like metabolism in
383 normal conditions, though showing signs of very early CAM evolution. The difference in
384 metabolism between both plants seems to be largely attained through regulatory rewiring of
385 functional enzymes.

386

387 **3.8. Circadian clock-related motif enrichment in promoter sequences**

388 We calculated the per-kb frequency of four known circadian clock-related motifs in the 2-
389 kb upstream regions of identified DE genes, to further understand the role of circadian clock
390 regulation in this set. We contrasted the frequencies of each motif in the set of DE genes against
391 their frequencies in upstream regions of non-DE genes, and found that the Evening Element (EE)
392 and CCA1-binding site (CBS) were the most enriched in this set with a frequency increase of 19
393 % and 18 % respectively (Table S8). The difference in median per-promotor count of these motifs
394 was however not statistically significant. Among co-expression clusters, the changes in motif
395 frequency compared to non-DE genes varied greatly. We find a significant increase in motif
396 frequency in cluster 1 for the G-Box motif (82 % increase), in cluster 3 for EE (207 %) and in
397 cluster 7 for CBS (43 %).

398 We performed the same analysis on a set of *T. leiboldiana* genes that were temporally
399 differentially expressed (see SI Note 10). The upstream regions of these genes also showed a small
400 but not statistically significant increase of 16 % and 10 % in EE and CBS frequency respectively.
401 The enrichment of circadian-clock related motifs in promotor regions of DE genes shows
402 similarities between the two species, with comparable rates of frequency change for each specific
403 element, though they are slightly larger in *T. fasciculata*.

When comparing the composition of circadian motifs in the upstream regions of core CAM genes and their homologs between species, we find a large diversity of motif presence among genes (Table S9), yet homologs between species tend to share the same motifs. No circadian motif appears to be present in any homolog of PEPC except for a copy in *T. leiboldiana* which was not differentially expressed between species. On the other hand, PPCK, an important regulator of PEPC, contains several circadian motifs, and shows marked differences in its composition compared to its non-DE homolog (PPCK1). The DE copy of PPCK misses two G-Box sites compared to its homolog in *T. leiboldiana*.

3.9. Genomic features of DE and CAM-related genes

3.9.1. Genomic distribution of DE genes is not associated with rearranged regions

Differentially expressed genes are present on all major scaffolds of both genome assemblies and the total number of DE genes per scaffold is positively correlated with the scaffold size (Kendall's correlation coefficient: 0.365 in *T. fasciculata* and 0.453 in *T. leiboldiana*, p-values < 0.015). Rearranged scaffolds in *T. leiboldiana* do not show a deviation in DE counts from other scaffolds relative to their size (Fig. S9). The density of DE genes is slightly higher in *T. fasciculata* than in *T. leiboldiana* (1.47 vs. 0.93 DE genes per 1-kb window on average). On the other hand, the average proportion of genes that are DE per 1-kb window is higher in *T. leiboldiana* (3.3 %) than in *T. fasciculata* (2.9 %), indicating that DE genes are more often located in gene-sparse regions in *T. leiboldiana* (Fig. S10).

3.9.2. Differentially expressed genes belong more often to multi-copy orthogroups

To investigate the consequences of gene family evolution on gene expression, we tested whether the proportion of multi-copy orthogroups underlying DE genes was significantly elevated to that of the whole-genome set of orthogroups in both species (Fig. 5b, SI Note 9). The 907 DE genes in *T. fasciculata* are found in 738 orthogroups (hereafter called DE orthogroups) containing a total of 2,141 and 910 genes in *T. fasciculata* and *T. leiboldian*a, respectively. Genes from multi-copy orthogroups are more likely to be differentially expressed: while multi-copy orthogroups account for 24 % of all orthogroups in the genome, they represent 31 % of DE orthogroups. This

difference is primarily explained by a 3.2x larger proportion of multi-copy orthogroups with a larger family size in *T. fasciculata* than in *T. leiboldiana* in the DE subset compared to the whole genome (Chi-square P = $1.59e^{-66}$).

Reciprocally, the DE analysis on the *T. leiboldiana* genome (SI Note 9) resulted in 836 DE genes belonging to 714 orthogroups, of which 489 overlap with the DE orthogroups resulting from the analysis on the *T. fasciculata* genome. As in the analysis on the *T. fasciculata* genome, we find that orthogroups with a larger family size in *T. leiboldiana* are enriched among DE genes. Additionally, both analyses point at a significant enrichment for multi-copy orthogroups with equal family sizes in both species, suggesting that also older duplications preceding the split of *T. fasciculata* and *T. leiboldiana* play a role in day-night regulatory evolution. This highlights the importance not only of novel, but also ancient variation in fuelling trait evolution in *Tillandsia*.

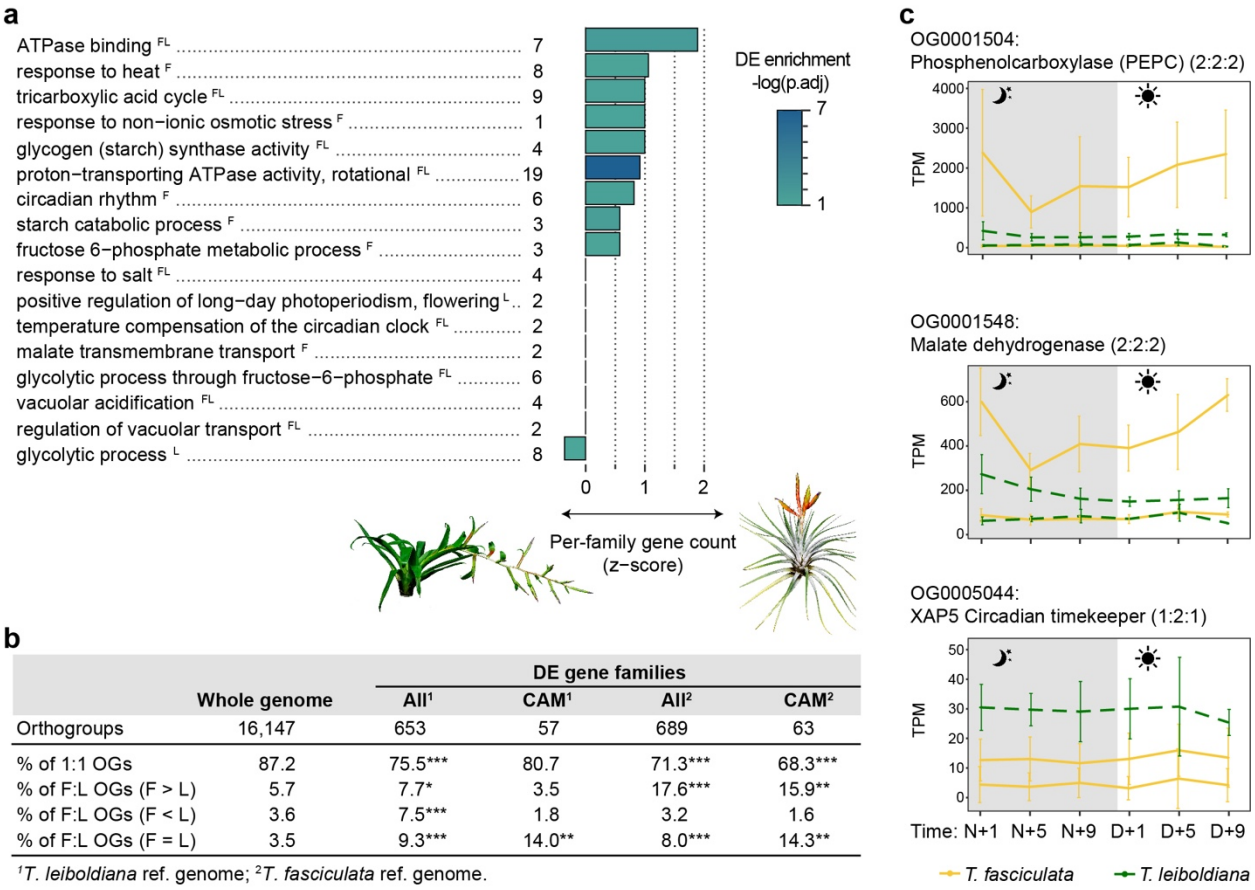

b

	Whole genome	DE gene families			
		All[1]	CAM[1]	All[2]	CAM[2]
Orthogroups	16,147	653	57	689	63
% of 1:1 OGs	87.2	75.5***	80.7	71.3***	68.3***
% of F:L OGs (F > L)	5.7	7.7*	3.5	17.6***	15.9**
% of F:L OGs (F < L)	3.6	7.5***	1.8	3.2	1.6
% of F:L OGs (F = L)	3.5	9.3***	14.0**	8.0***	14.3**

[1]*T. leiboldiana* ref. genome; [2]*T. fasciculata* ref. genome.

Figure 5: a) *CAM-related enriched GO terms among differentially expressed (DE) genes between* T. fasciculata *and* T. leiboldiana*. The genome in which a GO term has been found to be enriched among DE genes is shown by* ^{F} *and* ^{L} *for* T. fasciculata *and* T. leiboldiana*, respectively. The family size difference for the underlying orthogroups is represented as a Z-score*: a *negative score*

indicates a tendency towards gene families with larger size in T. leiboldiana *than in* T. fasciculata*, and vice versa. The p-value displayed represents the significance of the GO-term enrichment among DE genes in* T. fasciculata *unless the term was only enriched in* T. leiboldiana*. The number of DE genes underlying each function is shown next to the GO-term name.* ***b)*** *Composition of gene families by relative size between T. fasciculata (F) and T. leiboldiana (L) for three subsets of gene families (whole genome, DE, and CAM-related DE). Species-specific orthogroups are not included in this analysis. A chi-square test of independence was applied to test the significance of composition changes in 2x2 contingency tables for each category when testing the entire DE gene subset. For CAM DE genes, the Fisher's exact test was applied. Significant p-values of both tests are reported as: *0.05-0.01, **0.01-0.0001, ***0.0001-0.* ***c)*** *Expression profiles in a 24-hour period of exemplary CAM-related gene families (PEPC, MDH and XCT) displayed at the orthogroup level. For each gene copy and timepoint, the average read count (in Transcripts Per Million, TPM), and the standard deviation across accessions are displayed. Read counts of each ortholog are obtained by mapping conspecific accessions to their conspecific reference genome. We show two families with older duplications preceding the split of* T. fasciculata *and* T. leiboldiana *(PEPC and MDH) and one gene family with a recent duplication in* T. fasciculata *(XCT).*

Multi-copy gene families are also enriched in a restricted subset of DE orthogroups related to CAM, starch metabolism and gluconeogenesis (68 genes in 67 orthogroups), especially gene families with equal copy number and with copy number expansion in *T. fasciculata* (Fig. 5b, Table S5). Importantly, expanded gene families in *T. leiboldiana* are not significantly enriched in this functional subset, showing that while the full set of DE orthogroups exhibit increased gene family dynamics in both lineages, CAM-related gene family expansion is only associated with *T. fasciculata* (constitutive CAM). This pattern is also reflected on the GO-term level, where enriched CAM-related biological functions appear disproportionally associated with gene family expansion in *T. fasciculata* (nine functions) than in *T. leiboldiana* (one function). Functions associated with V-ATPase proton pumps especially tend to have larger gene family size in *T. fasciculata* than in *T. leiboldiana* (ATPase binding, proton-transporting ATPase activity).

CAM-related expanded gene families often show one highly expressed copy that performs diel cycling, while the other copies are lowly or not expressed (e.g. SDH, glyceraldehyde-3-

482 phosphate dehydrogenase (GAPDH), V-ATPase subunit H, SI Note 10), however, several gene
483 families show diel and/or elevated expression in *T. fasciculata* in two or more gene copies (starch
484 synthase, Ppi-dependent PFK and enolase, SI Note 10). Both copies of XCT are expressed in *T.*
485 *fasciculata,* though showing no diel cycling or increased expression compared to *T. leiboldiana*
486 (Fig. 5c), making its role in CAM photosynthesis unclear. V-ATPase subunit H has eight copies
487 in *T. fasciculata* and three in *T. leiboldiana*. While in both species only one copy is highly
488 expressed (with diel cycling peaking at night in *T. fasciculata*), the copies implemented for
489 elevated expression in either species are not each other's homologs (SI Note 10), suggesting that
490 different copies are recruited for the distinct photosynthetic phenotypes of these species. The other
491 copies are lowly or not expressed. A candidate gene family with larger gene family size in *T.*
492 *leiboldiana* is a probable aquaporin PIP2-6 (OG0005047, Fig. S11), which is involved in water
493 regulation and follows a diel pattern in pineapple (*A. comosus*) (Zhu and Ming, 2019). While lowly
494 expressed in *T. fasciculata*, one of the two gene copies shows strong diel expression in *T.*
495 *leiboldiana*, with highest expression in the early night. This is another indication that an early,
496 latent CAM cycle may be present in *T. leiboldiana*.
497 CAM-related gene families with duplications preceding the divergence of *T. leiboldiana*
498 and *T. fasciculata* include a malate dehydrogenase (MDH) with two copies in both species, where
499 only one copy is highly expressed and cycling in *T. fasciculata,* and the core CAM enzyme
500 Phosphoenolpyruvate carboxylase (PEPC), which shares an ancient duplication among monocots
501 (Deng et al., 2016) (Fig. 5c). The widely varying expression patterns of multicopy DE CAM-
502 related families suggest a variety of mechanisms possibly contributing to CAM regulatory
503 evolution: dosage changes ("more of the same"), subfunctionalization and neofunctionalization.
504

505 **3.9.3. Differentially expressed genes have more TE insertions**

506 To investigate whether transposable element (TE) activity and differential gene expression
507 are associated in *Tillandsia*, we tested whether TE insertions in introns and the 3-kb upstream
508 regions of genes are significantly enriched in DE genes in both species. Both the presence of one
509 or more TE insertions in a gene, as well as the average number of TE insertions per gene is higher
510 across all genes of *T. leiboldiana* compared to the *T. fasciculata* gene set, which was expected
511 given its larger proportion of repetitive content (See Results section 3.2.).

512 While in both genomes, the proportion of DE genes with one or more TE insertions is not
513 significantly different to that of the full gene set, the average number of TE insertions per gene is
514 significantly higher in DE compared to non-DE genes (Table 1).
515 On the other hand, TE insertion rates in DE genes related to CAM, starch metabolism and
516 glycolysis / gluconeogenesis do not significantly differ from background rates in both genomes,
517 though they are slightly reduced (Table 1). However, the proportion of CAM-related DE genes
518 with an intronic TE insertion is larger in *T. fasciculata* (41.2 %) than in *T. leiboldiana* (36.2 %),
519 despite *T. leiboldiana*'s generally elevated intronic TE insertion rate. This pattern is not discernible
520 when including TE insertions in the 3-kb upstream region of genes.
521

Table 1: Statistical test results on TE insertions in DE versus non-DE genes, and in DE genes previously described as underlying CAM, glycolysis, or starch metabolism, versus all other genes. TE insertions were counted in intronic + 3-kb upstream regions, but insertions in introns only are also shown. P-value: *>0.05, **>0.01, ***>10-3

Total number of genes with one or more TE insertions						
	T. fasciculata			*T. leiboldiana*		
	All genes	DE genes	CAM DE genes	All genes	DE genes	CAM DE genes
All TEs (intronic only)	15,844 (50 %)	473 (52 %)	28 (41.2 %)	10,348 (51 %)	387 (54 %)	21 (36.2 %)*
All TEs	22,969 (90 %)	725 (91 %)	58 (85 %)	18,512 (91 %)	665 (92 %)	50 (86 %)
DNA transposons	16,857 (66 %)	556 (70 %)	45 (66 %)	14,463 (71 %)	547 (76 %)**	42 (72 %)
Helitrons	17,388 (69 %)	561 (70 %)	47 (69 %)	14,701 (72 %)	530 (74 %)	38 (65 %)
LTR-Copia	11,147 (44 %)	353 (44 %)	28 (41 %)	10,487 (51 %)	394 (55 %)	31 (53 %)
LTR-Gypsy	10,365 (41 %)	341 (43 %)	22 (32 %)	5,399 (26 %)	199 (28 %)	10 (17 %)
Average and (median) TE insertion counts per gene						
	T. fasciculata			*T. leiboldiana*		
	non-DE genes	DE genes	CAM genes	non-DE genes	DE genes	CAM genes
All TEs (intronic only)	2.90 (1)	3.71 (1)*	2.618 (0)	3.24 (1)	3.96 (1)**	2.862 (0)
All TEs	6.79 (5)	7.83 (6)**	6.32 (5)	7.62 (5)	8.75 (6)***	7.36 (5)
DNA transposons	2.15 (1)	2.56 (2)***	2.03 (1)	2.49 (2)	2.97 (2)***	2.77 (2)
Helitrons	1.97 (1)	2.27 (2)***	2.12 (1)	2.43 (2)	2.72 (2)*	2.12 (1)
LTR-Copia	1.00 (0)	0.95 (0)	0.87 (0)	1.22 (1)	1.45 (1)**	1.25 (1)
LTR-Gypsy	0.92 (0)	1.09 (0)	0.76 (0)	0.61 (0)	0.65 (0)	0.39 (0)

522 When studying genic TE insertions across four separate TE classes, we recover a similar
523 trend among all categories as observed across all TEs. Insertion rates around genes are the highest
524 for DNA transposons in both species, but the TE class that is most often present around a gene are
525 Helitrons, which occur in 69 % and 72 % of genes in *T. fasciculata* and *T. leiboldiana* respectively
526 (Table 1). This contrasts with the small proportion of the whole genome that is covered by
527 Helitrons – only 5.86 % and 3.7 % in *T. fasciculata* and *T. leiboldiana* respectively (Table S3).
528 LTRs, while covering the largest proportion of the genome in both species, are the least present
529 and show the lowest insertion rates around genes in both species.
530 Nine DE genes related to CAM, starch, and gluconeogenesis display more than twice the
531 number of TE insertions as the genome-wide average in *T. fasciculata*. This includes a V-type
532 proton ATPase subunit H (vacuolar transport and acidification), an aluminium-activated malate
533 transporter, an ABC transporter C family member 4 (stomatal opening and circadian rhythm) and
534 a mitochondrial isocitrate dehydrogenase subunit (Table S10), which all had more TE insertions
535 than their orthologs in *T. leiboldiana*. On the other hand, six DE genes of interest had elevated TE
536 insertion rates in *T. leiboldiana,* including a vacuolar acid invertase (sugar metabolism) and a sugar
537 transporter ERD6-like. Four of these genes showed high amounts of TE insertions in both
538 genomes, such as a glucose-1-phosphate adenylyltransferase subunit (starch synthesis), a V-type
539 proton ATPase subunit C, and circadian clock regulator GIGANTEA (Dalchau et al., 2011), which
540 also plays a role in stomatal opening (Ando et al., 2013).
541
542 **4. Discussion**
543 The sources of variation fuelling trait evolution in rapid radiations have been a long-
544 standing topic in evolutionary biology (Simpson, 1953), and our understanding of how complex
545 traits such as CAM evolve repeatedly is still incomplete. By showcasing a broad range of
546 photosynthetic phenotypes and repeated evolution of constitutive CAM, the subgenus *Tillandsia*
547 provides an excellent opportunity to study CAM evolution. The recent divergence between
548 members of *Tillandsia* allows to pinpoint the necessary evolutionary changes to evolve a
549 constitutive CAM phenotype. By integrating comparative genomics using *de novo* assemblies and
550 in-depth gene expression analyses of two closely related *Tillandsia* species representing one of the
551 most distinct photosynthetic phenotypes within the clade, we found support for regulatory
552 evolution and gene family expansion as major features of CAM evolution (Fig. 6).

553 Our metabolic analyses of night-time malate accumulation and gene expression analyses
554 provide a much more detailed understanding of the photosynthetic phenotypes present in the
555 subgenus than the previously reported carbon isotope measurements, which do not accurately
556 reflect all stages of the CAM continuum. For example, weak CAM phenotypes have been reported
557 in Bromeliaceae for species with carbon isotope ratios falling in the C3 range (-26.5) (Pierce et al.,
558 2002), indicating that the photosynthetic metabolism of *T. leiboldiana* could be different from C3
559 *sensu stricto* as its carbon isotope measurements suggest. Our timewise malate measurements
560 show distinct fluxes for *T. fasciculata* and *T. leiboldiana*, with constitutive accumulation of night-
561 time malate in *T. fasciculata* which is absent in *T. leiboldiana*. On the other hand, *T. leiboldiana*
562 displays CAM-like temporal expression profiles for certain enzymes, such as PEPC kinase and
563 Aquaporin PIP-6, and shares circadian clock-related cis-elements in the promotor regions of CAM
564 homologs with *T. fasciculata*. It has been suggested that repeated evolution of CAM (similar to
565 C4) may be facilitated in lineages where C3 species already display increased or CAM-like
566 expression of core genes (Heyduk et al., 2019a, 2019b; Kajala et al., 2012). However, while a
567 CAM cycle is seemingly not being expressed in *T. leiboldiana* under normal circumstances, we
568 cannot exclude that a latent CAM cycle could become activated under certain conditions, for
569 example under drought stress. In that case, *T. leiboldiana* would rather be at the very early stages
570 of CAM evolution than a "pre-adapted" C3 plant (De La Harpe et al., 2020). We hope that future
571 studies will study the drought response of *T. leiboldiana* to better understand its exact position in
572 the CAM continuum.
573 On the other hand, even if *T. leiboldiana* and potentially all subgenus *Tillandsia* species
574 previously labelled as C3 represent in fact the early stages of the CAM continuum, our analyses
575 show widely distinct photosynthetic phenotypes within the radiation which required divergent
576 evolution. Therefore, while this study may underestimate the total number of evolutionary changes
577 needed to establish constitutive CAM from C3 *sensu stricto*, it highlights the evolutionary drivers
578 underlying the least understood section of the CAM continuum: from early CAM to constitutive
579 CAM.
580 Differences between the two genomes related to CAM evolution can be primarily found
581 on the regulatory level, with CAM-related genes showing temporal differential expression between
582 species across a 24-hour period. These reveal a complex web of underlying expression changes,
583 as they are distributed over all inferred co-expression clusters (Fig. S8). Together with the diversity

584 of circadian clock-related motif composition in promoter sequences (Table S8), this finding
585 emphasises the lack of a master regulator and a clear overall direction of expression changes
586 underlying CAM (Wickell et al., 2021; Heyduk et al., 2022).

587 Gene family expansion has been previously observed in CAM lineages (Cai et al., 2015;
588 Silvera et al., 2010) and suggested as a driver of CAM evolution (Silvera et al., 2014). We
589 witnessed an increased number of genes belonging to multi-copy families in *T. fasciculata* than in
590 *T. leiboldiana*, consistent with a net higher rate of gene duplication in this species than in *T.*
591 *leiboldiana*, as previously reported by De La Harpe et al. (2020). Strikingly, both the total subset
592 of differentially expressed genes and a more stringent group of CAM-related DE genes was
593 significantly enriched for gene families that have expanded in *T. fasciculata* (constitutive CAM).
594 CAM-related functions that were enriched in DE genes show a disproportionate bias towards gene
595 family expansion in *T. fasciculata* (circadian rhythm, vacuolar ATPase activity, tricarboxylic acid
596 cycle and starch metabolism) compared to *T. leiboldiana* (glycolysis) (Fig. 5a). Gene duplications,
597 preceding the split of *T. fasciculata* and *T. leiboldiana* are also significantly associated with day-
598 night expression differences in CAM-related genes (Fig. 5b), suggesting that older, already
599 existing gene duplications may also be recruited in CAM evolution, alongside novel duplications.

600 The expression curves of DE multicopy gene families with a potential link to CAM reveal
601 a multitude of expression behaviours (e.g. Fig. 5c), which supports that complex regulatory
602 evolution on the transcriptional level underlies CAM evolution. Our findings suggest that gene
603 family evolution played a significant role in modulating regulatory changes underlying the
604 evolution towards constitutive CAM in *Tillandsia*. As gene family expansion leads to increased
605 redundancy, selection on individual gene copies and their expression relaxes, facilitating the
606 assimilation of a constitutively expressed CAM expression profile (Ohno, 1970).

607 Another potential driver of trait evolution is TE insertion, though its role in CAM evolution
608 in *Tillandsia* remains unclear. TE insertions are overall less common in CAM-related DE genes
609 compared to all genes in both genomes, suggesting a selection pressure against TE insertions
610 around these genes. However, the proportion of CAM-related DE genes with intronic TE insertions
611 is greater in *T. fasciculata* than in *T. leiboldiana,* despite the overall higher genic TE insertion rate
612 in *T. leiboldiana*. This suggests that the pressure to maintain CAM-related genes TE-free is
613 reduced in the constitutive CAM lineage relative to *T. leiboldiana*. We detect nine and six CAM-
614 related DE genes with more than twice the whole-genome average TE insertion count in *T.*

615 *fasciculata* and *T. leiboldiana* respectively, of which four are single-copy orthologs shared
616 between species. The high degree of sharedness of TE-rich DE genes between species rather
617 suggests that TE insertions are not a major driver of CAM-related gene expression changes. In
618 fact, genes with exceptionally high insertion rates in *T. fasciculata* tend to show reduced
619 expression (ALMT, V-ATPase subunit H copy Tfasc_v1.24696, ABCC4, SI Note 10). Instead, the
620 larger proportion of CAM-related DE genes with one or more TE insertions in *T. fasciculata* may
621 be a consequence of higher rates of gene family expansion and eventual pseudogenization of
622 redundant copies.

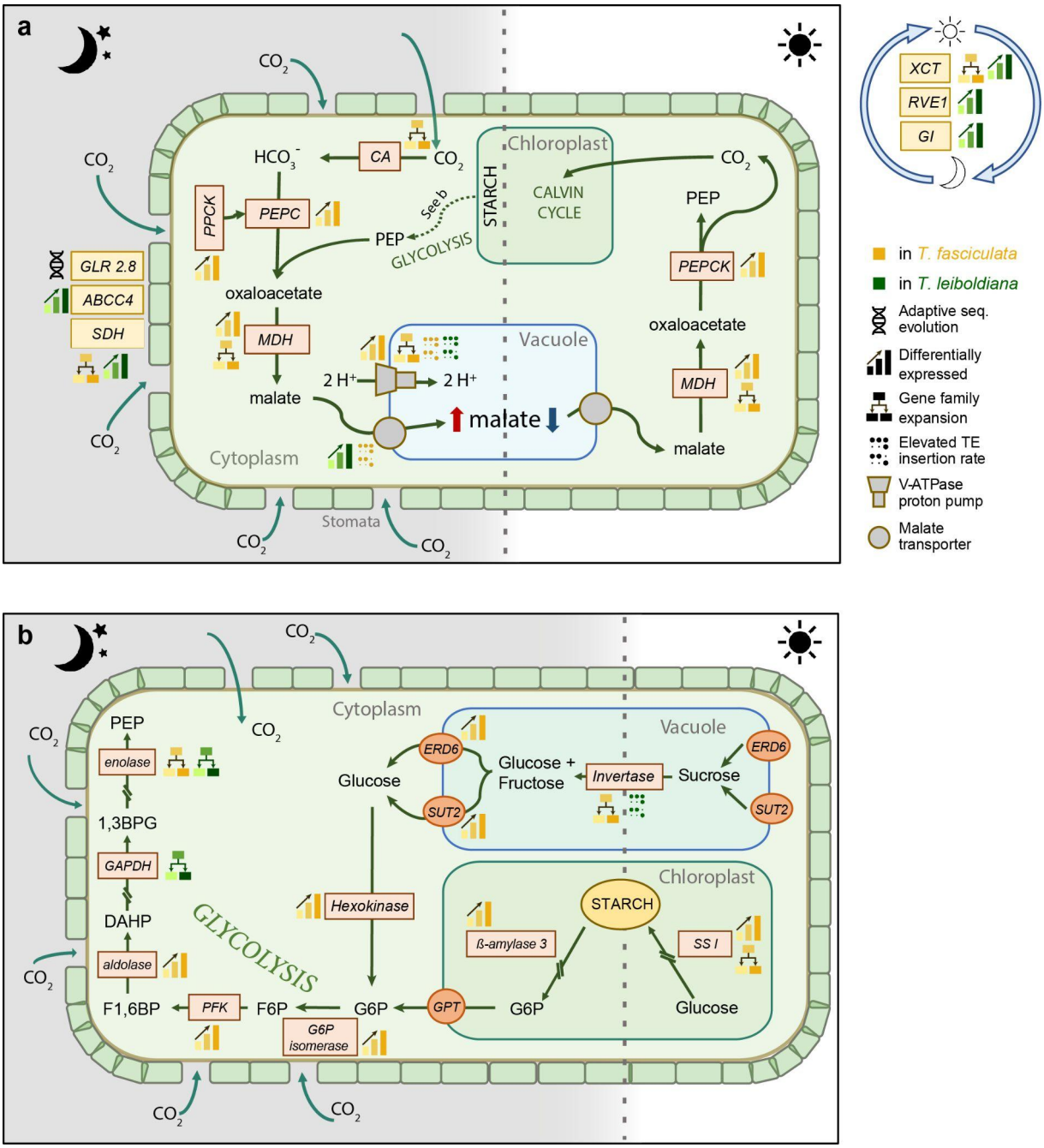

623

624 ***Figure 6:*** *Pathway of Crassulacean Acid Metabolism (CAM), highlighting underlying genes*
625 *detected in this study as differentially expressed, with gene family expansion, with signature of*
626 *adaptive sequence evolution or elevated TE insertion counts. The colour of the process indicates*
627 *the species showing diel or elevated expression, increased gene family size or increased TE*
628 *insertion rate. Enzymes are shown in coloured boxes, while pathway products are shown in bold*
629 *outside boxes. Enzymatic members of CAM metabolism pathways are shown in orange boxes,*
630 *while stomatal and circadian regulators are highlighted in yellow. Stomatal regulators are shown*

on the left outside the cell and circadian regulators on the right. ***a)*** *CO_2 is absorbed at night and first converted to HCO_3^- by carbonic anhydrase (CA). Then, it is converted to malate by carboxylating phosphoenolpyruvate (PEP), a key component of the glycolysis. In a first step, PEP carboxylase (PEPC) converts PEP to oxaloacetate, after being activated by PEPC kinase (PPCK). In a second step, malate dehydrogenase (MDH) converts oxaloacetate to malate. Malate is then transported into the vacuole by two possible transporters, either a tonoplast dicarboxylate transporter or an aluminium-activated malate transporter, which are assisted by V-ATPase proton pumps. During the day, the accumulated malate becomes the main source of CO_2 for photosynthesis. This allows the stomata to remain closed, which greatly enhances the water use efficiency of the plant. Malate is again transported out of the vacuole and reconverted to oxaloacetate by MDH, and then decarboxylated to PEP and CO_2 by PEP carboxykinase (PEPCK). The CO_2 will cycle through the Calvin cycle and generate sugars. Abbreviations: GLR2.8 – Glutamate receptor 2.8, ABCC4 - ABC transporter C 4, SDH – Succinate Dehydrogenase, XCT – XAP5 CIRCADIAN TIMEKEEPER, GI – protein GIGANTEA, RVE1 – REVEILLE 1.* ***b)*** *Glycolysis, transitory starch, and sugar metabolism are tightly linked with the core CAM pathway as providers of starting materials such as PEP. During the day, CAM plants can store starch in the chloroplast and hexoses in the vacuole. In Bromeliaceae, the relative importance of soluble sugars versus starch as a source for PEP is variable across species*[56]*. At night, the stored starch and/or sugars are transported into the cytoplasm, converted to glucose or fructose, and broken down via the glycolysis to PEP. Abbreviations: G6P - glucose-6-phosphate; PGM – phosphoglucomutase; GPT - glucose-6-phosphate/phosphate translocator; PFK – phosphofructokinase; GAPDH - Glyceraldehyde-3-phosphate dehydrogenase; F6P – fructose-6-phosphate; F1,6BP – fructose-1,6-biphosphate; SSI – starch synthase I; 1,3BPG - 1,3-Bisphosphoglyceric acid; PEP – Phosphoenolpyruvate; SUT2 – Sucrose transporter 2; ERD6 - EARLY RESPONSE TO DEHYDRATION 6. For a detailed description and accompanying per-gene expression profiles, see Fig. S6 and SI Note 10.*

Candidate genes under positive selection underlie a broad array of functions, but had no immediate link to CAM photosynthesis. While the study of adaptive sequence evolution would greatly benefit from a broader sampling across *Tillandsia*, the lack of overlap between regulatory and adaptive sequence evolution is in line with previously proposed mechanisms of CAM

evolution largely relying on regulatory changes in other systems (Deng et al., 2016). A small number of cases of convergent and adaptive sequence evolution between distantly related CAM and C3 species have been described (Yang et al., 2017), though no overlap was found between convergence in expression and sequence evolution. Our study suggests that while on larger evolutionary scales adaptive sequence evolution may play an important role, distinct photosynthetic phenotypes between closely related species may be achieved primarily with gene expression changes (but see SI Note 12), or may be especially relevant between the transition of C3 *sensu stricto* to the CAM continuum.

Though we observe a karyotype difference of six chromosome pairs between *T. fasciculata* and *T. leiboldiana* and we identified one fusion in the *T. leiboldiana* assembly, along with two reciprocal translocations, we did not find detectable consequences of large-scale rearrangements for either functional diversification or adaptation in *Tillandsia*, unlike other studies (Davey et al., 2016; Cicconardi et al., 2021) (Fig. 4b, S4, S6, but see SI Note 5 and 14). However, due to the remaining fragmentation of the *T. leiboldiana* genome, it is likely that we were not able to describe all rearrangements, and we hope that future endeavours will improve the genome assembly and make a more in-depth study of the role of large-scale rearrangements in the evolution of species barriers and/or the evolution of other key innovation traits in *Tillandsia possible*.

Our analyses reveal genomic changes of all scales between two members of an adaptive radiation representing a recent shift to constitutive CAM. However, in this recent shift between closely related species, differences in photosynthetic metabolism are brought about largely by temporal expression changes enabled by both existing and *de novo* gene duplication, rather than adaptive sequence evolution of existing gene copies, which may play a role at later stages of divergence (but see SI Note 12). Large scale rearrangements observed so far seem unlinked from functional divergence, more likely affecting reproductive isolation (de Vos et al., 2020; Faria and Navarro, 2010), and need further study. Our findings support an important role for gene family expansion in generating novel variation that fuels the evolution of the CAM continuum.

The two *de novo* assemblies presented in this study are the first tillandsioid and fourth bromeliad genomes published so far. Despite both genomes exhibiting one of the highest TE contents reported to date for a non-polyploid plant species (Pedro et al., 2021), the joint use of long-read sequencing and chromatin conformation capture successfully led to highly contiguous assemblies with high-quality gene sets (SI Note 13). Along with other recently developed

resources for Bromeliaceae (Yardeni et al., 2021; Liu et al., 2021), these genomes will be crucial in future investigations of this highly diverse and species-rich plant family, and in further studies of CAM evolution.

5. Materials & Methods

5.1. Flow cytometry and cytogenetic experiments

5.1.1. Genome size measurements

Approximately 25 mg of fresh leaf material was co-chopped according to the chopping method of (Galbraith et al., 1983) together with an appropriate reference standard (*Solanum pseudocapsicum*, 1.295 pg/1C) (Temsch, 2010; Temsch et al., 2022) in Otto´s I buffer (Otto et al., 1981). After filtration through a 30 µm nylon mesh (Saatilene Hitech, Sericol GmbH, Germany) and incubation with RNase A (0.15mg/ml, Sigma-Aldrich, USA) at 37°C, Otto´s II buffer (Otto et al., 1981) including propidium iodide (PI, 50mg/L, AppliChem, Germany) was added. Staining took place in the refrigerator for at least one hour or up to over-night. Measurement was conducted on a CyFlow ML or a CyFlow Space flow cytometer (Partec/Sysmex, Germany) both equipped with a green laser (532nm, 100mW, Cobolt AB, Sweden). The fluorescence intensity (FI) of 10,000 particles were measured per preparation and the 1C-value calculation for each sample followed the equation: $1C_{Obj} = (\text{FI peak mean}_{G1\ Obj} / \text{FI peak mean}_{G1\ Std}) \times 1C_{Std}$

5.1.2. Karyotyping

Actively growing root meristems of genome assembly accessions (see Table S1) were harvested and pre-treated with 8-hydroxyquinoline for 2 hours at room temperature and 2 hours at 4°C. The roots were then fixed in Carnoy's fixative (3 : 1 ethanol : glacial acetic acid) for 24 hours at room temperature and stored –20 °C until use. Chromosome preparations were made after enzymatic digestion of fixed root meristems as described in (Jang and Weiss-Schneeweiss, 2015). Chromosomes and nuclei were stained with 2 ng/µl DAPI (4',6-diamidino-2-2phenylindole) in Vectashield antifade medium (Vector Laboratories, Burlingame, CA, USA). Preparations were

723 analysed with an Axiolmager M2 epifluorescent microscope (Carl Zeiss) and images were
724 captured with a CCD camera using AxioVision 4.8 software (Carl Zeiss). Chromosome number
725 was established based on analyses of several preparations and at least five intact chromosome
726 spreads. Selected images were contrasted using Corel PhotoPaint X8 with only those functions
727 that applied equally to all pixels of the image and were then used to prepare karyotypes.
728

729 **5.2. Genome Assembly**

730

731 **5.2.1. Plant material selection and sequencing**

732 Genome assemblies were constructed from the plant material of one accession per species
733 (see Table S1). The accessions were placed in a dark room for a week to minimise chloroplast
734 activity and recruitment, after which the youngest leaves were collected and flash frozen with
735 liquid nitrogen. High molecular weight extraction for ultra-long reads, SMRTbell library
736 preparation and PacBio Sequel sequencing was performed by Dovetail Genomics™ (now Cantata
737 Bio). Dovetail Genomics™ also prepared Chicago (Putnam et al., 2016) and Hi-C (Lieberman-
738 Aiden et al., 2009) libraries which were sequenced as paired-end 150bp reads on an Illumina HiSeq
739 X instrument. Additional DNA libraries were prepared for polishing purposes using Illumina's
740 TruSeq PCR-free kit, which were sequenced on a HiSeq2500 as paired-end 125 bp reads at the
741 Vienna BioCenter Core Facilities (VBCF), Austria.

742 RNA-seq data of *T. fasciculata* used for gene annotation was sampled, sequenced, and
743 analysed in De La Harpe et al. 2020 under SRA BioProject PRJNA649109. For gene annotation
744 of *T. leiboldiana*, we made use of RNA-seq data obtained during a similar experiment, where
745 plants were kept under greenhouse conditions and sampled every 12 hours in a 24-hour cycle.
746 Importantly, while the *T. fasciculata* RNA-seq dataset contained three different genotypes, only
747 clonal accessions were used in the *T. leiboldiana* experiment. For *T. leiboldiana*, total RNA was
748 extracted using a QIAGEN RNeasy® Mini Kit, and poly-A capture was performed at the Vienna
749 Biocenter Core Facilities (VBCF) using a NEBNext kit to produce a stranded mRNA library. This
750 library was sequenced on a NovaSeq SP as 150 bp paired end reads.

751 For both species, sequencing data from different time points and accessions were merged
752 into one file for the purpose of gene annotation. Before mapping, the data was quality-trimmed

using AdapterRemoval (Schubert et al., 2016) with default options (--trimns, --trimqualities). We allowed for overlapping pairs to be collapsed into longer reads.

5.2.2. First draft assembly and polishing

We constructed a draft assembly using long-read PacBio data with CANU v1.8 (Koren et al., 2017) for both species. To mitigate the effects of a relatively low average PacBio coverage (33x), we ran two rounds of read error correction with high sensitivity settings (corMhapSensitivity=high corMinCoverage=0 corOutCoverage=200) for *T. fasciculata.* Additionally, we applied high heterozygosity (correctedErrorRate=0.105) settings, since K-mer based analyses pointed at an elevated heterozygosity in this species (See SI Note 2), and memory optimization settings (corMhapFilterThreshold=0.0000000002 corMhapOptions=" --repeat-idf-scale 50" mhapMemory=60g mhapBlockSize=500).

Given that the coverage of *T. leiboldiana* PacBio averaged 40x, we limited error correction for this species to only one round. CANU was run with additional settings accommodating for high frequency repeats (ovlMerThreshold=500) and high sensitivity settings as mentioned above.

To minimise the retention of heterozygous sequences as haplotigs in *T. fasciculata* (see SI Note 2), we reassigned allelic contigs using the pipeline Purge Haplotigs (Roach et al., 2018). Raw PacBio data was mapped to the draft assembly produced in the previous step with minimap2 (Li, 2018), before using the Purge Haplotigs pipeline.

Since the size of the *T. leiboldiana* draft assembly indicates, together with previous analyses, that this species is largely homozygous (SI Note 2), we did not include a PurgeHaplotigs step. However, we did make use of the higher average coverage of the *T. leiboldiana* PacBio data to polish the assembly with two rounds of PBMM v.1.0 and Arrow v2.3.3 (Pacific Biosciences).

5.2.3. Scaffolding and final polishing

Scaffolding of both assemblies was performed in-house by Dovetail Genomics™ using Chicago and Hi-C data and the HiRise scaffolding pipeline (Putnam et al., 2016). To increase base quality and correct indel errors, we ran additional rounds of polishing with high-coverage Illumina data (See above, section 2.1.) using Pilon v1.22 (Walker et al., 2014). The Illumina data was aligned to the scaffolded assembly using BWA-MEM (Li, 2013), and then Pilon was run on these alignments. We evaluated the result of each round using BUSCO v.3 (Waterhouse et al., 2018)

784 with the Liliopsida odb9 library and proceeded with the best version. For *T. fasciculata*, polishing
785 was performed twice, fixing SNPs and indels. We did not fix small structural variation in this
786 genome due to the relatively low coverage (35x) of Illumina data. For *T. leiboldiana*, one round
787 of polishing on all fixes (SNPs, indels and small structural variants) resulted in the highest BUSCO
788 scores.
789
790 **5.3. Annotation**
791
792 **5.3.1. TE annotation and repeat masking**
793 *De novo* TE annotation of both genome assemblies was performed with EDTA v.1.8.5 (Ou
794 et al., 2019) with option –sensitive. To filter out genes that have been wrongly assigned as TEs, *A.*
795 *comosus* (pineapple) coding sequences (Ming et al., 2015) were used in the final steps of EDTA.
796 Using the species-specific TE library obtained from EDTA, we masked both genomes
797 using RepeatMasker v.4.0.7 (Smit et al., 2013-2015). Importantly, we excluded all TE annotations
798 marked as "unknown" for masking to prevent potentially genic regions flagged as TEs to be
799 masked during annotation. The search engine was set to NCBI (-e ncbi) and simple and low-
800 complexity repeats were left unmasked (-nolow). We produced both hard-masked and soft-masked
801 (--xsmall) genomes.
802
803 **5.3.2. Transcriptome assembly**
804 We constructed transcriptome assemblies for both species using Trinity *de novo* assembler
805 v.2.4.8. (Grabherr et al., 2011) using default parameters starting from the raw mRNA-seq data.
806 These were evaluated with BUSCO. Additionally, before feeding the transcriptome assemblies to
807 the gene annotation pipeline, we ran a round of masking of interspersed repeats to avoid an
808 overestimation of gene models due to the presence of active transposases in the RNA-seq data.
809
810 **5.3.3. Gene prediction and functional annotation**
811 Gene models were constructed using a combination of BRAKER v.2.1.5 (Hoff et al., 2019)
812 and MAKER2 v.2.31.11 (Campbell et al., 2014). Starting with BRAKER, we obtained splicing
813 information from RNA-seq alignments to the masked genome as extrinsic evidence using the
814 *bam2hints* script of AUGUSTUS v.3.3.3 (Stanke et al., 2008). A second source of extrinsic

evidence for BRAKER were single-copy protein sequences predicted by BUSCO when run on the masked genomes in genome mode with option --long. Predictions made by BRAKER were evaluated with BUSCO and with RNA-seq alignments.

Subsequently, we built our final gene predictions using MAKER2. As evidence, we used (1) the gene models predicted by BRAKER, (2) a transcriptome assembly of each respective species (see above section 3.2.), (3) a protein sequence database containing proteins of *Ananas comosus comosus* (F153) (Ming et al., 2015) and *Ananas comosus bracteatus* (CB5) (Chen et al., 2019) and manually curated SwissProt proteins from monocot species (64,748 sequences in total) and (4) a GFF file of complex repeats obtained from the masked genome (see above section 3.1.) and an extended repeat library containing both the EDTA-produced *Tillandsia*-specific repeats and the monocot repeat library from RepBase (7,857 sequences in total). By only providing masking information of complex repeats and setting the model organism to "simple" in the repeat masking options, hard-masking in MAKER2 was limited to complex repeats while simple repeats were soft-masked, which makes these available for gene prediction. MAKER2 predicts genes both *ab initio* and based on the given evidence using AUGUSTUS.

We evaluated the resulting set of predicted gene models by mapping the RNA-seq data (section 2.1.) back to both the transcript and full gene model sequences and running BUSCO in transcriptome mode. We also calculated the proportion of masked content in these gene models to ascertain that MAKER2 had not predicted TEs as genes. A second run of MAKER, which included training AUGUSTUS based on the predicted models from the first round, resulted in lower BUSCO scores and was not further used. We functionally annotated the final set of gene models in Blast2Go v.5.2.5 (Götz et al., 2008) using the Viridiplantae database.

5.4. Inferring gene orthology

Orthology between gene models of *T. fasciculata*, *T. leiboldiana* and *Ananas comosus* was inferred using Orthofinder v.2.4.0 (Emms and Kelly, 2019). Protein sequences produced by MAKER2 of inferred gene models were used for *T. fasciculata* and *T. leiboldiana*. For *A. comosus*, the publicly available gene models of F153 were used. The full Orthofinder pipeline was run without additional settings. Counts per orthogroup and the individual genes belonging to each orthogroup were extracted from the output file Phylogenetic_Hierarchical_Orthogroups/N0.tsv.

845 Orthofinder was run a second time on gene models present only on main contigs (See
846 Results). For each gene model, the longest isoform was selected, and gene models with protein
847 sequences shorter than 40 amino acids were removed. This resulted in 27,024, 30,091 and 31,194
848 input sequences for *A. comosus*, *T. fasciculata* and *T. leiboldiana* respectively. Then, the steps
849 mentioned above were repeated.
850
851 **5.5. Gene model assessment and curation**
852 Gene model sets were assessed and curated using several criteria. Gene models with
853 annotations indicating a repetitive nature (transposons and viral sequences) together with all their
854 orthologs were marked with "NO_ORTHOLOGY" in the GFF file and excluded from downstream
855 analyses. Using the per-exon expression data obtained in our mRNA-seq experiment (see below,
856 section 11) and information gathered on the length of the CDS and the presence / absence of a start
857 and stop codon, we further classified our gene models into ROBUST and NOT-ROBUST
858 categories. A gene model was considered ROBUST (i) if all exons are expressed or, (ii) if both
859 start and stop codons are present and the CDS has a minimum length of 50 amino-acids.
860
861 **5.6. Analysing TE class abundances**
862 By rerunning EDTA with step --anno, we obtained TE abundances and detailed annotation
863 of repetitive content for the whole assembly. Per-contig abundances of each class were calculated
864 with a custom python script (available at https://github.com/cgrootcrego/Tillandsia_Genomes).
865 Using this curated TE library, the assemblies were masked again with RepeatMasker for
866 downstream analyses. The resulting TE class abundances reported by RepeatMasker were then
867 compared between species and reported.
868
869 **5.7. Spatial distribution of repetitive, genic and GC content**
870 The spatial distribution of genes, transposable elements and GC content as shown in Fig.
871 3a, was analysed on a per-window basis, using windows of 1 Mb. Gene counts were quantified as
872 the number of genes starting in every window, based on genes with assigned orthology, including
873 both single and multicopy gene models. Repetitive content was measured as the proportion of
874 masked bases in each window, stemming from the hard-masked assembly using the curated TE
875 library. Per-window gene counts and proportion of repetitive bases was then visualised using the

876 R package circlize (Gu et al., 2014). GC content was calculated as the proportion of G and C bases
877 per 1 Mb windows. Correlation between genic, repetitive and GC content was calculated and tested
878 for significance using the Kendall Rank Correlation Coefficient, after testing for normality using
879 the Shapiro-Wilk test.

880 Repetitive, GC and gene content as shown in Fig. 3b was estimated directly from the soft-
881 masked reference genomes using 100 kb non-overlapping sliding windows as described in (Leroy
882 et al., 2021). TE content corresponds to the proportion of soft-masked positions per window. For
883 the *Tillandsia* genomes, the curated TE library (see above, section 6.) was used as a basis for soft-
884 masking in RepeatMasker. For *A. comosus*, a soft-masked version of the genome was obtained
885 from NCBI (https://www.ncbi.nlm.nih.gov/datasets/genome/GCA_902162155.2/). As compared
886 to the version of Leroy et al. 2021, this script was modified to estimate GC content in repetitive
887 regions (soft-masked regions only). In addition to this, we estimated the genic fraction by
888 considering the total number of genomic positions falling in genes based on the GFF files (feature
889 = "gene") divided by the size of the window (100 kb). This estimate was derived for the same
890 window boundaries as used for GC and TE content to be able to compare all statistics. The relative
891 per-window proportion of genic bases corresponding to non-robust genes (see above, section 5)
892 was also estimated by dividing the number of non-robust gene positions with the total number of
893 gene positions.

894

895 **5.8. Synteny between *T. fasciculata* and *T. leiboldiana***

896 Synteny was inferred with GENESPACE v.0.8.5 (Lovell et al., 2022), using orthology
897 information obtained with Orthofinder of the gene models from *A. comosus*, *T. fasciculata* and *T.*
898 *leiboldiana*. This provided a first, visual graphical to detect large-scale rearrangements. We used
899 GENESPACE with default parameters, except that we generated the syntenic map (riparian plot)
900 using minGenes2plot=200. Other methods have also been used to confirm the chromosomal
901 rearrangements and to identify the genomic breakpoints more precisely (see SI Note 5).

902

903 **5.9. Gene family evolution**

904

905 **5.9.1. Family size correction**

906 Gene counts per orthogroup were evaluated using per-gene mean coverage to detect co-
907 assembled heterozygous gene sequences that may have escaped Purge Haplotigs in the assembly
908 step. To do this, whole-genome Illumina reads of both species (See Methods, section 2.1.) were
909 aligned to their respective assemblies using Bowtie2 v.2.4.4. (Langmead and Salzberg, 2012) with
910 the very-sensitive-local option. Bowtie2 specifically assigns multi-mapping reads randomly,
911 allowing the detection of artificial gene models thanks to a decreased overall coverage across the
912 orthogroup, as reads from one biological copy would be randomly distributed over two or more
913 locations in the genome. Per-base coverage in genic regions was calculated using *samtools depth*
914 and a bed-file specifying all locations of orthologous genes. We then calculated the average
915 coverage per orthologous gene.

916 The distribution of per-gene mean coverage in each species' gene model set was then
917 visualised using ggplot2 (Wickham, 2016) for different categories of genes: single-copy (only one
918 gene model assigned to the orthogroup in the species investigated), multi-copy (more than one
919 gene assigned to the orthogroup in the species investigated), ancestral single-copy (only one gene
920 model assigned to the orthogroup in all species used in the orthology analysis), ancestral multi-
921 copy (multiple gene model assigned to the orthogroup in all species used in the orthology analysis
922 and the number of gene models assigned is equal across species), and unique multi-copy (more
923 than one gene assigned to the orthogroup in the species investigated and no genes assigned to the
924 orthogroup in other species). This revealed that, while most categories of genes had a unimodal
925 distribution centred around the average coverage across the genome, multi-copy and unique multi-
926 copy families showed a bimodal or expanded distribution, especially in *T. fasciculata* (Fig. S12).
927 This points at the presence of genes with multiple alleles per gene in the annotation. Hence, gene
928 count sizes per orthogroup and species were corrected by the ratio of the total coverage across all
929 genes of one species in the orthogroup and the expected coverage, which was calculated as the
930 product of the total number of genes in the orthogroup and the average coverage of single-copy
931 genes in that species.

932 Size corrections were only applied on orthogroups containing multicopy genes. Plastid and
933 mitochondrial genes were excluded from this analysis. We detected plastid genes with BLASTn
934 against the *A. comosus* chloroplast sequence and the *Oryza* IRSGP-1 mitochondrial sequence.

935 Additionally, all genes annotated as "ribosomal" were also excluded from the downstream gene
936 family evolution analyses.
937 Originally, 9,210 genes in *T. fasciculata* and 6,257 genes in *T. leiboldiana* were assigned
938 to orthogroups with multiple gene copies in at least one species. After correcting orthogroup sizes
939 by coverage, we retained 6,261 and 4,693 gene models, respectively (Table S4).
940
941 **5.9.2. Analysis of multicopy orthogroups**

942 The distribution of gene counts per multicopy orthogroup was compared between *T.*
943 *fasciculata* and *T. leiboldiana* with a non-parametric test (Mann-Whitney U). Using the log-ratio
944 of per-species gene count, we investigated which gene families experienced large changes in gene
945 count compared to the background (SI Note 6).
946 Functional characterization of multicopy families was done with a GO term enrichment
947 analysis of the underlying genes using the Fisher's exact test in TopGo (Alexa and Rahnenführer,
948 2009). Enrichment analyses were done on all genes belonging to multicopy orthogroups, on a
949 subset of genes belonging to families that are larger in *T. fasciculata* and on a subset of genes
950 belonging to families that are larger in *T. leiboldiana*. The top 100 significantly enriched GO terms
951 were then evaluated. GO terms putatively associated with key innovation traits were used to list
952 multicopy gene families of interest.
953 Additionally, we searched for specific genes that are known to underlie CAM evolution in
954 these multi-copy gene families. The IDs of candidate pineapple genes for CAM were obtained
955 from (Yardeni et al., 2021), who compiled extensive lists of genes from a diverse set of studies.
956 For CAM, we considered all genes listed in Table S1 in this study under the categories
957 "Differentially expressed in CAM / C3 experiment" (186 genes) (De La Harpe et al., 2020),
958 "Positive selection in CAM / C3 shifts" (22) (De La Harpe et al., 2020), Gene families associated
959 with CAM/C3" (79) (De La Harpe et al., 2020), "CAM-related *A. comosus*" (29) (Ming et al.,
960 2015), "stomatal function" (48) (Christin et al., 2014), "aquaporin regulation" (24) (Vera-Estrella
961 et al., 2012), "drought resistance" (61) (Xiao et al., 2007), "circadian metabolism" (47) (Wai et al.,
962 2017), "malate transferase" (28) (Cosentino et al., 2013) and "circadian clock" (3) (McClung,
963 2006), resulting in a total of 527 genes. A separate list was made for gluconeogenesis and starch
964 metabolism genes (288 genes) (Cushman et al., 2008). After obtaining these lists of pineapple gene

965 IDs, we searched for their orthologs in *T. fasciculata* and *T. leiboldiana*, and investigated their
966 presence in multi-copy gene families.
967
968 **5.10. d_N/d_S analysis**
969
970 **5.10.1. On single-copy orthologous pairs**
971 One-to-one orthologous genes were subjected to a test of positive selection using the non-
972 synonymous to synonymous substitution ratio ($\omega = d_N/d_S$). Gene pairs where both genes were
973 incomplete (missing start and/or stop codon) or where the difference in total length was more than
974 20 % of the length of either gene were removed. We performed codon-aware alignments using the
975 alignSequences program from MACSE v.2.05 (Ranwez et al., 2018) with options -
976 local_realign_init 1 -local_realign_dec 1 for optimization. Pairwise d_N/d_S ratios were estimated
977 with the codeML function of PAML v.4.9. (Yang, 2007). Using a single-ratio model across sites
978 and branches (Nssites = 0, model = 0), we tested for a fixed $\omega = 1$ as null hypothesis, against an
979 unfixed ω as the alternative hypothesis. Automatisation of codeML was achieved with a modified
980 script from AlignmentProcessor (https://github.com/WilsonSayresLab/AlignmentProcessor/). The
981 results of codeML under both the null and alternative model were compiled and significance of
982 the result was calculated with the likelihood-ratio test (Wong et al., 2004). Multiple-testing
983 correction was applied with the Benjamini-Hochberg method and an FDR threshold of 0.05.
984 Orthologous gene pairs with a d_N/d_S ratio larger than one and an adjusted p-value under 0.05 were
985 considered candidate genes under divergent selection.
986 The d_N/d_S values of all orthologous gene pairs with five or more variant sites in the MACSE
987 alignment were used to obtain per-scaffold distributions of d_N/d_S values in both genomes. We
988 visualised d_N/d_S distributions of all main scaffolds in both assemblies with boxplots and used
989 density plots to visualise the d_N/d_S distribution in rearranged chromosomes compared to all non-
990 rearranged chromosomes. To test whether these distributions were significantly different, we ran
991 a non-parametric test (Mann-Whitney U) between the distribution of each single rearranged
992 chromosome and that of all non-rearranged chromosomes in each assembly.
993

994 #### 5.10.2. On duplicated orthogroups

995 We also performed tests of selection using d_N/d_S on all orthogroups that were consisted of
996 a single gene in *A. comosus* and a duplicated gene in either T. *leiboldiana* (1:1:2), or *T. fasciculata*
997 (1:2:1). Only orthogroups that maintained this conformation after size correction were used in this
998 analysis. Pairwise alignments were performed between the ortholog of one species and either
999 paralog of the other species using MACSE. Then, ω was estimated in the same way as mentioned
1000 above.
1001

1002 ### 5.11. RNA-seq experiment capturing photosynthetic phenotypes and expression
1003

1004 #### 5.11.1. Experiment set-up and sampling

1005 To capture gene expression patterns related to CAM, we designed an RNA-seq experiment
1006 where individuals of *T. fasciculata* and *T. leiboldiana* were sampled at six time points throughout
1007 a 24-hour cycle. Six plants of each species were placed in a PERCIVAL climatic cabinet at 22 °C
1008 and a relative humidity (rH) of 68 % for 4 weeks, with a 12-hour light cycle. Light was provided
1009 by fluorescent lamps with a spectrum ranging from 400 to 700 nm. The light intensity was set at
1010 124 $\mu mol/m^2s$. The plants acclimated to these conditions for 4 weeks prior to sampling, during
1011 which they were watered every second day.

1012 Leaf material from each plant was sampled every 4 hours in a 24-hour cycle starting one
1013 hour after lights went off. One leaf was pulled out of the base at each time-point without cutting.
1014 The base and tip of the leaf were then removed, and the middle of the leaf immediately placed in
1015 liquid nitrogen, then stored at -80 °C.
1016

1017 #### 5.11.2. Targeted metabolite analyses

1018 To corroborate the photosynthetic phenotypes of *T. fasciculata* and *T. leiboldiana*, we
1019 measured malate abundances in the leaf throughout a 24-hour cycle. An approximate amount of
1020 20 mg of frozen leaf material collected at six timepoints during the above-mentioned experiment
1021 was collected and ground to a powder with a TissueLyser and metal beads. Subsequent steps were
1022 performed at the Vienna Metabolomics Center (VIME, Department of Ecogenomics and Systems
1023 Biology, Vienna, Austria).

1024 Polar metabolites were extracted in three randomised batches by modifying the procedure
1025 of (Weckwerth et al., 2004). A weighed amount of deep frozen and ground plant tissues was
1026 combined with 750 µL of ice-cold extraction solvent, consisting of methanol (LC-MS grade,
1027 Merck), chloroform (anhydrous >99 %, Sigma Aldrich), and water (MilliQ) in a ratio of 2.5:1:0.5
1028 (v/v). Additionally, 7 µL of a solution of 10 mmol of pentaerythritol (PE) and 10 mM phenyl-β-d-
1029 glucopyranoside (PGP) respectively in water (MilliQ) were added as an internal standard mix.
1030 After ultrasonication at 4 °C for 20 minutes and centrifugation (4 min, 4 °C, 14,000 g) the
1031 supernatant was transferred to a new 1.5 mL tube (polypropylene). Another 250 µL of extraction
1032 solvent was added to the remaining pellet and after another cycle of ultrasonication and
1033 centrifugation as described before, the supernatant was combined with the previous. To induce
1034 phase separation 350 µL of water (MilliQ) was added. After thorough mixing and consecutive
1035 centrifugation (4 min, 4 °C, 14,000 g) 900 µL of the upper phase were transferred to a new 1.5 mL
1036 tube. Approximately 100 µL of the remaining polar phase of all samples were combined. The
1037 900 µL aliquotes of this mixed sample were used as quality control during measurements. The
1038 polar phases and the aliquotes of the sample mix were dried in a vacuum centrifuge for 5 hours at
1039 30 °C and 0.1 mbar.
1040 The dried extracts were derivatised as described earlier (Doerfler et al., 2013) by dissolving
1041 the metabolite pellet carefully in 20 µL of 40 mg of methoxyamine hydrochloride (Sigma Aldrich)
1042 in 1 mL pyridine (anhydrous >99,8 %, Sigma Aldrich). After incubation at 30 °C and 700 rpm for
1043 1.5 hours on a thermoshaker, 80 µL of *N*-methyl-*N*-trimethylsilyl-trifluoroacetamid (Macherey-
1044 Nagel) were added. The samples were incubated for 30 min at 37 °C and 750 rpm and
1045 consecutively centrifuged for 4 min at room temperature and 14,000 g.
1046 Metabolite analysis was performed on an Agilent 7890B gas chromatograph equipped with
1047 a LECO Pegasus® BT-TOF mass spectrometer (LECO Corporation). Derivatised metabolites
1048 were injected through a Split/Splitless inlet equipped with an ultra-inert single tapered glass liner
1049 with deactivated glass wool (5910-2293, Agilent Technologies), a split ratio of 1:25 was used and
1050 the temperature was set to 230 °C. Components were separated with helium as carrier gas on a
1051 Restek Rxi-5Sil MS column (length: 30 m, diameter: 0.25 mm, thickness of film: 0.25 µm). The
1052 initial oven temperature was set to 70 °C held for 1 minute and ramped with a rate of 9 °C per
1053 minute until reaching 340 °C held for 10 minutes. Collection of spectra started after an acquisition
1054 delay of 280 seconds with a detector voltage of 1692.5 V, a rate of 15 spectra per second and a

1055 mass range of 50−500 *m/z*. Retention indices were calculated based on the retention times of the
1056 alkane mixture C_{10}-C_{40} run within each of the 2 batches. Samples were measured in randomised
1057 order and randomly distributed across the batches. Within each batch, a mixture of standard
1058 metabolites was measured for MSI level I identification of metabolites. Deconvolution, annotation,
1059 and processing of chromatograms was performed according to (Zhang et al., 2023) using
1060 ChromaTOF® (Version 5.55.29.0.1187, LECO Cooperation) and MS-DIAL, version 4.7
1061 (Tsugawa et al., 2015). Areas of derivatisation products of single metabolite were summed and
1062 normalised by the main targeted ion content of each sample.
1063

1064 **5.11.3. RNA extraction and sequencing**

1065 Using the same sampled leaf material as for targeted metabolite analyses, total RNA was
1066 extracted for each sample and timepoint in randomised batches of 4-6 samples, using the QIAGEN
1067 RNeasy® Mini Kit in an RNAse free laboratory. Samples were digested using the kit's RLT buffer
1068 with 1 % Beta-mercaptoethanol. Elution was done in two steps. The purity and concentration of
1069 the extractions was measured using Nanodrop, and RIN and fragmentation profiles were obtained
1070 with a Fragment Analyzer™ system. RNA libraries were prepared by the Vienna Biocenter Core
1071 Facilities (VBCF) using a NEBNext stranded mRNA kit before sequencing 150-bp paired-end
1072 reads on one lane of Illumina NovaSeq S4.
1073

1074 **5.11.4. RNA-seq data processing**

1075 The raw RNA-seq data was evaluated with FastQC
1076 (https://www.bioinformatics.babraham.ac.uk/projects/fastqc/) and MultiQC (Ewels et al., 2016),
1077 then quality trimmed using AdapterRemoval v.2.3.1 (Schubert et al., 2016) with settings --trimns
1078 --trimqualities --minquality 20 --trimwindows 12 --minlength 36. The trimmed data was then
1079 aligned to both the *T. fasciculata* and *T. leiboldiana* genomes using STAR v.2.7.9 (Dobin et al.,
1080 2013) using GFF files to specify exonic regions. Because mapping bias was lowest when mapping
1081 to *T. fasciculata* (see SI Note 8, Fig. S13, S14), our main analyses have been performed on the
1082 reads mapped to this genome. However, the alignments to *T. leiboldiana* were used for verification
1083 or expansion of the main analysis (SI Note 9).
1084

1085 **5.11.5. Differential Gene Expression analysis**

1086 We quantified read counts per exon using FeatureCounts from the Subread package v.2.0.3.
1087 (Liao et al., 2014) for paired-end and reversely stranded reads (-p -s 2). The counts were then
1088 summed up across exons per gene to obtain gene-level counts. The composition of the count data
1089 was investigated with PCA in EdgeR (Robinson et al., 2009). Then, counts were normalised using
1090 the TMM method in EdgeR, and every gene with a mean cpm < 1 was removed. We ran a
1091 differential gene expression (DE) analysis in maSigPro (Conesa et al., 2006), which detects genes
1092 with differential diurnal expression profiles between species using a regression approach. *T.*
1093 *leiboldiana* was used as the baseline in this analysis. Significant DE genes were then clustered
1094 using the hclust algorithm into modules, with the number of modules being determined with the
1095 K-means algorithm. Expression curves were plotted by taking the average expression in TPM
1096 (Transcripts per Million) across all replicates per species at each time. We calculated TPM by
1097 dividing the raw read count by the exonic length of the gene (RPK), which we then divided by the
1098 total sum of RPK values. Expression curves for entire clusters (Fig. S8) were plotted by median-
1099 centring the log(TPM) of each gene and time point against the median of all genes at each time
1100 point, while expression curves for individual genes or gene families (Fig. 5c, S5, S7) report average
1101 TPM.

1102 GO term enrichments were performed for each cluster using the R package TopGO (Alexa
1103 and Rahnenführer, 2009). Separately, known candidate genes underlying CAM and starch
1104 metabolism (See Methods, Section 5.9.) were searched among differentially expressed genes.

1105

1106 **5.11.6. Annotation and enrichment of circadian clock-related motifs in**
1107 **promoter sequences**

1108

1109 We counted the occurrences of four known circadian clock-related motifs in the 2-kb upstream
1110 regions of DE genes: the Morning Element (MOE: CCACAC) (Michael et al., 2008), the Evening
1111 Element (EE: AAAATATC) (Hudson and Quail, 2003), the CCA1-binding site (CBS:
1112 AAAAATCT) (Franco-Zorrilla et al., 2014) and the G-box element (G-box: CACGTG) (Michael
1113 and McClung, 2002). The same was done for all other curated genes that were not DE, which we
1114 considered as background sequences. We calculated the per-kb frequency of each motif based on

1115 the counts and total promoter length (2000 x number of genes) for both sets of genes. The
1116 percentage of change in frequency was calculated between both sets for each motif. Significance
1117 of frequency changes of circadian motifs in promotor regions of DE genes compared to non-DE
1118 genes were calculated with the Wilcoxon Rank Sum Test.

1119 For a small set of genes known to underly key CAM enzymes, we counted the occurrence
1120 of each motif in both the 2-kb upstream region of every homolog of that gene (including non-DE
1121 paralogs) in both species, to annotate and describe circadian motifs in promoter sequences in detail.
1122 The detection of motifs was extended to 3-kb regions to allow for a more distant presence of motifs.
1123

1124 5.12. Intersecting findings of gene family evolution, TE insertion ad differential 1125 gene expression

1126

1127 5.12.1. Spatial distribution of DE genes

1128 The previously calculated per 1 kb-window counts of robust genes was used to obtain the per-
1129 window proportion of DE genes. This was then visualised with circlize as described above.
1130 Correlations of total DE gene count per scaffold and scaffold size was calculated with Kendall's
1131 rank correlation test after testing for normality with the Shapiro-Wilk test.
1132

1133 5.12.2. Gene family evolution and differential gene expression

1134

1135 Orthogroups were split based on relative family size in *T. fasciculata* (F) versus *T.*
1136 *leiboldiana* (L) in the following categories: Single-copy orthogroups (F = 1 : L = 1), orthogroups
1137 with family size larger in *T. fasciculata* (F > L), orthogroups with family size smaller in *T.*
1138 *fasciculata* (F < L), orthogroups with equal family sizes that are larger than 1 (F = L). Orthogroups
1139 unique to one species (F:0 or 0:L) were not considered in this analysis. We counted the number of
1140 orthogroups belonging to each category for the full orthogroup set, for the subset of orthogroups
1141 containing DE genes (DE orthogroups) and for the subset of orthogroups containing DE genes that
1142 have been previously described as CAM-related (CAM-DE orthogroups). We then tested whether
1143 counts in each orthogroup category were enriched in DE orthogroups and CAM-DE orthogroups
1144 compared to all orthogroups. For comparisons of all orthogroups versus DE orthogroups, we used
1145 the chi-square test of independence in R. For the comparison of CAM-DE orthogroups versus all
1146 orthogroups, we used Fisher's exact test due to small sample sizes with 2x2 contingency tables of

1147 each orthogroup category versus all other categories, and DE genes versus non-DE genes. To study
1148 the effect of the reference genome used on our findings on gene family evolution in DE genes, we
1149 performed the same analysis on read counts obtained from mapping to *T. leiboldiana* (SI Note 9).
1150

1151 ### 5.12.3. Transposable element insertions and differential gene expression

1152 Intronic TE insertions were obtained using *bedtools intersect* on the GFF files of the TE
1153 and gene annotations of both species. We used the full transcript length of a gene (feature =
1154 "mRNA" in GFF file) for this analysis, and only applied "known" TE annotations and the set of
1155 curated genes. This resulted in a dataset reporting the number of TE insertions per gene. We also
1156 obtained TE counts for genic regions including the 3-kb upstream region, by using *bedtools slop*
1157 with options *-l 3000 -r 0 -s*. For analyses on specific TE classes, we calculated TE insertion counts
1158 for the following four TE categories: LTR-Copia, LTR-Gypsy, Helitron and DNA transposon.

1159 We then performed two tests on the resulting TE counts per gene: (1) whether the
1160 proportion of genes with one or more TE insertions is elevated in DE genes compared to the full
1161 gene set (chi-square test), and (2) whether the rate of TE insertions per gene measured, as the total
1162 count of intersections for each gene annotation with a TE annotation, is elevated in DE genes
1163 compared to non-DE genes (Mann-Whitney U test).

1164 The same test was also applied to a restricted set of DE genes previously described as
1165 CAM-related, or involved in starch metabolism and gluconeogenesis. Then, genes of interest with
1166 a TE insertion rate higher than twice the genome-wide average were selected and the difference in
1167 number of TE insertions between orthologs of *T. leiboldiana* and *T. fasciculata* was taken in case
1168 of a one-to-one relationship.
1169

1170 ## 6. Accession Numbers

1171 The genome assemblies and raw data used in this study are available at NCBI-SRA under
1172 BioProject PRJNA927306. Specifically, the *T. fasciculata* genome assembly TFas_v1 can be
1173 downloaded here: https://ncbi.nlm.nih.gov/datasets/genome/GCA_029168755.1/. The *T.*
1174 *leiboldiana* genome assembly TLei_v1 can be found at:
1175 https://www.ncbi.nlm.nih.gov/datasets/genome/GCA_029204045.1/. The annotation of both
1176 genomes is available on the Github repository at:
1177 https://github.com/cgrootcrego/Tillandsia_Genomes, together with the list of orthogroups, counts

1178 table used for RNA-seq analyses, full GO term enrichment results, and all scripts written for this
1179 manuscript. The *A. comosus* sequences used in this study stem from BioProject PRJNA371634
1180 (F153): https://www.ncbi.nlm.nih.gov/bioproject/PRJNA371634/ and BioProject PRJNA747096
1181 (CB5): https://www.ncbi.nlm.nih.gov/bioproject/PRJNA747096. Information on all accessions
1182 used in this study can be found in Supplemental Table 1.
1183

1184 **7. Supplemental data**

1185 Supplemental Figure S1. Per-metabolite loadings of PC1 and PC2
1186 Supplemental Figure S2. Distribution of scaffold sizes and orthologous gene counts for the top
1187 100 largest scaffolds of both assemblies.
1188 Supplemental Figure S3. TE, GC, and gene content at three examples of syntenic chromosome
1189 triplets.
1190 Supplemental Figure S4. In-depth visualisation of large-scale rearrangements between *T.*
1191 *fasciculata* and *T. leiboldiana.*
1192 Supplemental Figure S5. Genome-wide distribution of d_N/d_S values between single-copy
1193 orthologous genes.
1194 Supplemental Figure S6. Heatmap of z-score normalised expression values (log(TPM)) of CAM-
1195 related DE genes featured in Figure 6.
1196 Supplemental Figure S7. Average expression curve of PEPC kinase (PPCK) in *T. fasciculata* and
1197 *T. leiboldiana.*
1198 Supplemental Figure S8. Per-gene expression curves of all differentially expressed genes clustered
1199 in co-expression modules.
1200 Supplemental Figure S9: Relationship between DE gene count per scaffold and scaffold size.
1201 Supplemental Figure S10. Distribution of DE genes across the genome.
1202 Supplemental Figure S11. Average expression curve of Aquaporin 2-6 in *T. fasciculata* and *T.*
1203 *leiboldiana.*
1204 Supplemental Figure S12. Distribution of mean per-gene coverage across different gene family
1205 categories.
1206 Supplemental Figure S13. Unique mapping rates of RNA-seq reads to three different reference
1207 genomes.

1208 Supplemental Figure S14. Multi-mapping rates of RNA-seq reads to three different reference
1209 genomes.
1210 Supplemental Figure S15. Genome size measurement histograms.
1211 Supplemental Figure S16. Mitotic metaphase chromosomes and karyotypes of *Tillandsia*
1212 *fasciculata* and *Tillandsia leiboldiana.*
1213 Supplemental Figure S17. Heterozygosity and genome size estimation with a k-mer based
1214 approach.
1215 Supplemental Figure S18. Distribution of heterozygous sites per 1000 mappable variants.
1216 Supplemental Table S1. List of accessions used in this study.
1217 Supplemental Table S2. Assembly statistics.
1218 Supplemental Table S3. TE Abundances.
1219 Supplemental Table S4. Orthology statistics.
1220 Supplemental Table S5. List of CAM-related expanded orthogroups.
1221 Supplemental Table S6. Full list of candidate genes under positive selection.
1222 Supplemental Table S7. Full list of co-expression modules.
1223 Supplemental Table S8. Per-kb frequencies of four promoter motifs associated with circadian
1224 clock transcription factors in DE and non-DE genes.
1225 Supplemental Table S9. Annotation of circadian promoter motifs in the upstream regions of CAM
1226 genes.
1227 Supplemental Table S10. List of DE genes related to CAM, starch metabolism and
1228 gluconeogenesis with a high TE insertion rate.
1229 Supplemental File 1. Supplementary Notes.
1230 Supplemental Dataset 1. Metabolomic Compound Abundances reported as raw area read-outs
1231 from MS-Dial, including the level of identification according to the Metabolomics Standards
1232 Initiative.
1233

1234 **8. Acknowledgments**

1235 *In memory of Christian Lexer – we will treasure your enthusiasm, guidance, and memory always*.
1236 This work was financially supported by the Austrian Science Fund (FWF) through the doctoral
1237 programme (DK) grant W1225-B20 to a faculty team including C.L. and O.P., FWF grant P35275
1238 to O.P., and by the professorship start-up grant of Christian Lexer at the University of Vienna

BE772002. We thank Joachim Hermisson, Magnus Nordborg, Andrew Clark, Nicholas Barton, Virginie Courtier-Orgogozo, John Parsch, Andreas Futschik, Rui Borges, Aglaia Szukala, Florian Schwarz, Marta Pelizzolla and Ahmad Muhammad for insightful discussions, advice, and feedback. We thank Gert Bachmann and Eline de Vos for help with the setup of the RNA-seq experiment; Peter Bak, Andreas Franzke, Nils Köster and Helmut & Lieselotte Hromadnik for their generous donations of *Tillandsia* accessions; and Thelma Barbarà for assistance during RNA extractions. We also thank Barbara Knickmann, Viktor Vagovics and Manfred Speckmaier for the care of *Tillandsia* plants at the Botanical Garden of the University of Vienna. Lastly, we thank Alisa Tscherko for assistance with trichome photography. Computational resources were provided by the Life Science Computer Cluster (LiSC) of the University of Vienna and the Vienna Scientific Cluster.

9. Author Contributions

This study was conceived by CL, JH, OP, TL and CGC. Sampling was conducted by MHJB, WT, GY and MDH. Laboratory work was conducted by MHJB, SS, LACS and CGC. Cytogenetic work was performed by HWS and EMT. The RNA-Seq experiment and DE analysis was conducted by CGC under the guidance of KH and OP. Analyses were performed by CGC, JH, GY, TL, and FB. The manuscript was primarily written by CGC and amended following the dedicated reading and feedback of all co-authors, especially KH, TL, and OP.

10. References

Alexa, A. and Rahnenführer, J. (2009). Gene set enrichment analysis with topGO. Bioconductor Improv **27**: 1–26.

Ando, E., Ohnishi, M., Wang, Y., Matsushita, T., Watanabe, A., Hayashi, Y., Fujii, M., Ma, J.F., Inoue, S.-I., and Kinoshita, T. (2013). TWIN SISTER OF FT, GIGANTEA, and CONSTANS have a positive but indirect effect on blue light-induced stomatal opening in Arabidopsis. Plant Physiol. **162**: 1529–1538.

Araújo, W.L. et al. (2011). Antisense inhibition of the iron-sulphur subunit of succinate dehydrogenase enhances photosynthesis and growth in tomato via an organic acid-mediated effect on stomatal aperture. Plant Cell **23**: 600–627.

Arnegard, M.E., Zwickl, D.J., Lu, Y., and Zakon, H.H. (2010). Old gene duplication facilitates origin and diversification of an innovative communication system—twice. Proceedings of the National Academy of Sciences **107**: 22172–22177.

1273 **Baduel, P., Quadrana, L., Hunter, B., Bomblies, K., and Colot, V.** (2019). Relaxed purifying
1274 selection in autopolyploids drives transposable element over-accumulation which provides
1275 variants for local adaptation. Nat. Commun. **10**: 5818.

1276 **Barfuss, M.H.J., Till, W., Leme, E.M.C., Pinzón, J.P., Manzanares, J.M., Halbritter, H.,**
1277 **Samuel, R., and Brown, G.K.** (2016). Taxonomic revision of bromeliaceae subfam.
1278 Tillandsioideae based on a multi-locus DNA sequence phylogeny and morphology.
1279 Phytotaxa **279**: 1–97.

1280 **Benzing, D.H. and Bennett, B.** (2000). Bromeliaceae: Profile of an Adaptive Radiation
1281 (Cambridge University Press).

1282 **Borland, A.M., Hartwell, J., Weston, D.J., Schlauch, K.A., Tschaplinski, T.J., Tuskan, G.A.,**
1283 **Yang, X., and Cushman, J.C.** (2014). Engineering crassulacean acid metabolism to
1284 improve water-use efficiency. Trends Plant Sci. **19**: 327–338.

1285 **Bräutigam, A., Schlüter, U., Eisenhut, M., and Gowik, U.** (2017). On the Evolutionary Origin
1286 of CAM Photosynthesis. Plant Physiol. **174**: 473–477.

1287 **Brawand, D. et al.** (2015). The genomic substrate for adaptive radiation in African cichlid fish.
1288 Nature **513**: 375–381.

1289 **Brown, G.K. and Gilmartin, A.J.** (1989). Chromosome Numbers in Bromeliaceae. Am. J. Bot.
1290 **76**: 657–665.

1291 **Cai, J. et al.** (2015). The genome sequence of the orchid Phalaenopsis equestris. Nat. Genet. **47**:
1292 65–72.

1293 **Campbell, M.S., Holt, C., Moore, B., and Yandell, M.** (2014). Genome Annotation and Curation
1294 Using MAKER and MAKER-P. Curr. Protoc. Bioinformatics **2014**: 4.11.1-4.11.39.

1295 **Carnal, N.W. and Black, C.C.** (1989). Soluble Sugars as the Carbohydrate Reserve for CAM in
1296 Pineapple Leaves : Implications for the Role of Pyrophosphate:6-Phosphofructokinase in
1297 Glycolysis. Plant Physiol. **90**: 91–100.

1298 **Chen, L.-Y. et al.** (2019). The bracteatus pineapple genome and domestication of clonally
1299 propagated crops. Nat. Genet. **51**: 1549–1558.

1300 **Cheng, Y., Zhou, W., El Sheery, N.I., Peters, C., Li, M., Wang, X., and Huang, J.** (2011).
1301 Characterization of the Arabidopsis glycerophosphodiester phosphodiesterase (GDPD)
1302 family reveals a role of the plastid-localized AtGDPD1 in maintaining cellular phosphate
1303 homeostasis under phosphate starvation. Plant J. **66**: 781–795.

1304 **Christin, P.-A., Arakaki, M., Osborne, C.P., Bräutigam, A., Sage, R.F., Hibberd, J.M., Kelly,**
1305 **S., Covshoff, S., Wong, G.K.-S., Hancock, L., and Edwards, E.J.** (2014). Shared origins
1306 of a key enzyme during the evolution of C4 and CAM metabolism. J. Exp. Bot. **65**: 3609–
1307 3621.

1308 **Cicconardi, F., Lewis, J.J., Martin, S.H., Reed, R.D., Danko, C.G., and Montgomery, S.H.**

1309 (2021). Chromosome Fusion Affects Genetic Diversity and Evolutionary Turnover of
1310 Functional Loci but Consistently Depends on Chromosome Size. Mol. Biol. Evol. **38**:
1311 4449–4462.

1312 **Conesa, A., Nueda, M.J., Ferrer, A., and Talón, M.** (2006). maSigPro: a method to identify
1313 significantly differential expression profiles in time-course microarray experiments.
1314 Bioinformatics **22**: 1096–1102.

1315 **Cosentino, C., Di Silvestre, D., Fischer-Schliebs, E., Homann, U., De Palma, A., Comunian,**
1316 **C., Mauri, P.L., and Thiel, G.** (2013). Proteomic analysis of Mesembryanthemum
1317 crystallinum leaf microsomal fractions finds an imbalance in V-ATPase stoichiometry
1318 during the salt-induced transition from C3 to CAM. Biochem. J. **450**: 407–415.

1319 **Crayn, D.M., Winter, K., Schulte, K., and Smith, J.A.C.** (2015). Photosynthetic pathways in
1320 Bromeliaceae: Phylogenetic and ecological significance of CAM and C3 based on carbon
1321 isotope ratios for 1893 species. Bot. J. Linn. Soc. **178**: 169–221.

1322 **Crayn, D.M., Winter, K., and Smith, J.A.C.** (2004). Multiple origins of crassulacean acid
1323 metabolism and the epiphytic habit in the Neotropical family Bromeliaceae. Proceedings
1324 of the National Academy of Sciences **101**: 3703–3708.

1325 **Cushman, J.C.** (2001). Crassulacean acid metabolism. A plastic photosynthetic adaptation to arid
1326 environments. Plant Physiol. **127**: 1439–1448.

1327 **Cushman, J.C., Tillett, R.L., Wood, J.A., Branco, J.M., and Schlauch, K.A.** (2008). Large-
1328 scale mRNA expression profiling in the common ice plant, Mesembryanthemum
1329 crystallinum, performing C3 photosynthesis and Crassulacean acid metabolism (CAM). J.
1330 Exp. Bot. **59**: 1875–1894.

1331 **Dalchau, N., Baek, S.J., Briggs, H.M., Robertson, F.C., Dodd, A.N., Gardner, M.J.,**
1332 **Stancombe, M.A., Haydon, M.J., Stan, G.-B., Gonçalves, J.M., and Webb, A.A.R.**
1333 (2011). The circadian oscillator gene *GIGANTEA* mediates a long-term response of the
1334 *Arabidopsis thaliana* circadian clock to sucrose. Proc. Natl. Acad. Sci. U. S. A. **108**: 5104–
1335 5109.

1336 **Davey, J.W., Chouteau, M., Barker, S.L., Maroja, L., Baxter, S.W., Simpson, F., Merrill,**
1337 **R.M., Joron, M., Mallet, J., Dasmahapatra, K.K., and Jiggins, C.D.** (2016). Major
1338 Improvements to the Heliconius melpomene Genome Assembly Used to Confirm 10
1339 Chromosome Fusion Events in 6 Million Years of Butterfly Evolution. G3 **6**: 695–708.

1340 **De La Harpe, M. et al.** (2020). Genomic footprints of repeated evolution of CAM photosynthesis
1341 in a Neotropical species radiation. Plant Cell Environ. **43**: 2987–3001.

1342 **Deng, H., Zhang, L.-S., Zhang, G.-Q., Zheng, B.-Q., Liu, Z.-J., and Wang, Y.** (2016).
1343 Evolutionary history of PEPC genes in green plants: Implications for the evolution of CAM
1344 in orchids. Mol. Phylogenet. Evol. **94**: 559–564.

1345 **Dobin, A., Davis, C.A., Schlesinger, F., Drenkow, J., Zaleski, C., Jha, S., Batut, P., Chaisson,**
1346 **M., and Gingeras, T.R.** (2013). STAR: Ultrafast universal RNA-seq aligner.

Bioinformatics **29**: 15–21.

Doerfler, H., Lyon, D., Nägele, T., Sun, X., Fragner, L., Hadacek, F., Egelhofer, V., and Weckwerth, W. (2013). Granger causality in integrated GC–MS and LC–MS metabolomics data reveals the interface of primary and secondary metabolism. Metabolomics **9**: 564–574.

Edwards, E.J. (2023). Reconciling continuous and discrete models of C4 and CAM evolution. Ann. Bot.

Emms, D.M. and Kelly, S. (2019). OrthoFinder: Phylogenetic orthology inference for comparative genomics. Genome Biol. **20**: 238.

Ewels, P., Magnusson, M., Lundin, S., and Käller, M. (2016). MultiQC: summarize analysis results for multiple tools and samples in a single report. Bioinformatics **32**: 3047–3048.

Faria, R. and Navarro, A. (2010). Chromosomal speciation revisited: rearranging theory with pieces of evidence. Trends Ecol. Evol. **25**: 660–669.

Franco-Zorrilla, J.M., López-Vidriero, I., Carrasco, J.L., Godoy, M., Vera, P., and Solano, R. (2014). DNA-binding specificities of plant transcription factors and their potential to define target genes. Proc. Natl. Acad. Sci. U. S. A. **111**: 2367–2372.

Galbraith, D.W., Harkins, K.R., Maddox, J.M., Ayres, N.M., Sharma, D.P., and Firoozabady, E. (1983). Rapid flow cytometric analysis of the cell cycle in intact plant tissues. Science **220**: 1049–1051.

Gitaí, J., Paule, J., Zizka, G., Schulte, K., and Benko-Iseppon, A.M. (2014). Chromosome numbers and DNA content in Bromeliaceae: Additional data and critical review. Bot. J. Linn. Soc. **176**: 349–368.

Givnish, T.J. et al. (2014). Adaptive radiation, correlated and contingent evolution, and net species diversification in Bromeliaceae. Mol. Phylogenet. Evol. **71**: 55–78.

Götz, S., García-Gómez, J.M., Terol, J., Williams, T.D., Nagaraj, S.H., Nueda, M.J., Robles, M., Talón, M., Dopazo, J., and Conesa, A. (2008). High-throughput functional annotation and data mining with the Blast2GO suite. Nucleic Acids Res. **36**: 3420–3435.

Grabherr, M.G. et al. (2011). Full-length transcriptome assembly from RNA-Seq data without a reference genome. Nat. Biotechnol. **29**: 644–652.

Gu, Z., Gu, L., Eils, R., Schlesner, M., and Brors, B. (2014). Circlize implements and enhances circular visualization in R. Bioinformatics **30**: 2811–2812.

Hayashi, S., Ishii, T., Matsunaga, T., Tominaga, R., Kuromori, T., Wada, T., Shinozaki, K., and Hirayama, T. (2008). The glycerophosphoryl diester phosphodiesterase-like proteins SHV3 and its homologs play important roles in cell wall organization. Plant Cell Physiol. **49**: 1522–1535.

1382 **Heyduk, K., McAssey, E.V., and Leebens-Mack, J.** (2022). Differential timing of gene
1383 expression and recruitment in independent origins of CAM in the Agavoideae
1384 (Asparagaceae). New Phytol. **235**: 2111–2126.

1385 **Heyduk, K., Moreno-Villena, J.J., Gilman, I.S., Christin, P.-A., and Edwards, E.J.** (2019a).
1386 The genetics of convergent evolution: insights from plant photosynthesis. Nat. Rev. Genet.
1387 **20**: 485–493.

1388 **Heyduk, K., Ray, J.N., Ayyampalayam, S., Moledina, N., Borland, A., Harding, S.A., Tsai,**
1389 **C.-J., and Leebens-Mack, J.** (2019b). Shared expression of crassulacean acid metabolism
1390 (CAM) genes pre-dates the origin of CAM in the genus Yucca. J. Exp. Bot. **70**: 6597–6609.

1391 **Hoang, N.V. et al.** (2023). The Gynandropsis gynandra genome provides insights into whole-
1392 genome duplications and the evolution of C4 photosynthesis in Cleomaceae. Plant Cell **35**:
1393 1334–1359.

1394 **Hoff, K.J., Lomsadze, A., Borodovsky, M., and Stanke, M.** (2019). Whole-genome annotation
1395 with BRAKER. In Gene prediction (Humana: New York), pp. 65–95.

1396 **Holtum, J.A.M., Smith, J.A.C., and Neuhaus, H.E.** (2005). Intracellular transport and pathways
1397 of carbon flow in plants with crassulacean acid metabolism. Funct. Plant Biol. **32**: 429–
1398 449.

1399 **Hudson, M.E. and Quail, P.H.** (2003). Identification of promoter motifs involved in the network
1400 of phytochrome A-regulated gene expression by combined analysis of genomic sequence
1401 and microarray data. Plant Physiol. **133**: 1605–1616.

1402 **Jang, T.-S. and Weiss-Schneeweiss, H.** (2015). Formamide-Free Genomic in situ Hybridization
1403 Allows Unambiguous Discrimination of Highly Similar Parental Genomes in Diploid
1404 Hybrids and Allopolyploids. Cytogenet. Genome Res. **146**: 325–331.

1405 **Kajala, K., Brown, N.J., Williams, B.P., Borrill, P., Taylor, L.E., and Hibberd, J.M.** (2012).
1406 Multiple Arabidopsis genes primed for recruitment into C_4 photosynthesis. Plant J. **69**: 47–
1407 56.

1408 **Katju, V. and Bergthorsson, U.** (2013). Copy-number changes in evolution: rates, fitness effects
1409 and adaptive significance. Front. Genet. **4**: 273.

1410 **Kong, D. et al.** (2016). L-Met Activates Arabidopsis GLR Ca2+ Channels Upstream of ROS
1411 Production and Regulates Stomatal Movement. Cell Rep. **17**: 2553–2561.

1412 **Koren, S., Walenz, B.P., Berlin, K., Miller, J.R., Bergman, N.H., and Phillippy, A.M.** (2017).
1413 Canu: scalable and accurate long-read assembly via adaptive k-mer weighting and repeat
1414 separation. Genome Res. **27**: 722–736.

1415 **Leroy, T., Anselmetti, Y., Tilak, M.-K., Bérard, S., Csukonyi, L., Gabrielli, M., Scornavacca,**
1416 **C., Milá, B., Thébaud, C., and Nabholz, B.** (2021). A bird's white-eye view on avian sex
1417 chromosome evolution. Peer Community Journal **1**.

1418 **Li, H.** (2013). Aligning sequence reads, clone sequences and assembly contigs with BWA-MEM.
1419 arXiv [q-bio.GN].

1420 **Li, H.** (2018). Minimap2: pairwise alignment for nucleotide sequences. Bioinformatics **34**: 3094–
1421 3100.

1422 **Liao, Y., Smyth, G.K., and Shi, W.** (2014). FeatureCounts: An efficient general purpose program
1423 for assigning sequence reads to genomic features. Bioinformatics **30**: 923–930.

1424 **Lieberman-Aiden, E. et al.** (2009). Comprehensive mapping of long-range interactions reveals
1425 folding principles of the human genome. Science **326**: 289–293.

1426 **Liu, L., Li, X., Yuan, L., Zhang, G., Gao, H., Xu, X., and Zhao, H.** (2022). XAP5 CIRCADIAN
1427 TIMEKEEPER specifically modulates 3' splice site recognition and is important for
1428 circadian clock regulation partly by alternative splicing of LHY and TIC. Plant Physiol.
1429 Biochem. **172**: 151–157.

1430 **Liu, L., Tumi, L., Suni, M.L., Arakaki, M., Wang, Z.-F., and Ge, X.-J.** (2021). Draft genome
1431 of Puya raimondii (Bromeliaceae), the Queen of the Andes. Genomics **113**: 2537–2546.

1432 **Lovell, J.T., Sreedasyam, A., Schranz, M.E., Wilson, M., Carlson, J.W., Harkess, A., Emms,**
1433 **D., Goodstein, D.M., and Schmutz, J.** (2022). GENESPACE tracks regions of interest
1434 and gene copy number variation across multiple genomes. Elife **11**: e78526.

1435 **Lowry, D.B. and Willis, J.H.** (2010). A widespread chromosomal inversion polymorphism
1436 contributes to a major life-history transition, local adaptation, and reproductive isolation.
1437 PLoS Biol. **8**.

1438 **Luo, J., Sun, X., Cormack, B.P., and Boeke, J.D.** (2018). Karyotype engineering by
1439 chromosome fusion leads to reproductive isolation in yeast. Nature **560**: 392–396.

1440 **Males, J.** (2018). Concerted anatomical change associated with crassulacean acid metabolism in
1441 the Bromeliaceae. Funct. Plant Biol. **45**: 681–695.

1442 **McClung, C.R.** (2006). Plant circadian rhythms. Plant Cell **18**: 792–803.

1443 **McGee, M.D., Borstein, S.R., Meier, J.I., Marques, D.A., Mwaiko, S., Taabu, A., Kishe, M.A.,**
1444 **O'Meara, B., Bruggmann, R., Excoffier, L., and Seehausen, O.** (2020). The ecological
1445 and genomic basis of explosive adaptive radiation. Nature **586**: 75–79.

1446 **McRae, S.R., Christopher, J.T., Smith, J.A.C., and Holtum, J.A.M.** (2002). Sucrose transport
1447 across the vacuolar membrane of Ananas comosus. Funct. Plant Biol. **29**: 717–724.

1448 **Messerschmid, T.F.E., Wehling, J., Bobon, N., Kahmen, A., Klak, C., Los, J.A., Nelson, D.B.,**
1449 **dos Santos, P., de Vos, J.M., and Kadereit, G.** (2021). Carbon isotope composition of
1450 plant photosynthetic tissues reflects a Crassulacean Acid Metabolism (CAM) continuum
1451 in the majority of CAM lineages. Perspect. Plant Ecol. Evol. Syst. **51**: 125619.

1452 **Michael, T.P. et al.** (2008). Network Discovery Pipeline Elucidates Conserved Time-of-Day–

1453 Specific cis-Regulatory Modules. PLoS Genet. **4**: e14.

1454 **Michael, T.P. and McClung, C.R.** (2002). Phase-specific circadian clock regulatory elements in
1455 Arabidopsis. Plant Physiol. **130**: 627–638.

1456 **Ming, R. et al.** (2015). The pineapple genome and the evolution of CAM photosynthesis. Nat.
1457 Genet. **47**: 1435–1442.

1458 **Mondragón-Palomino, M. and Theissen, G.** (2009). Why are orchid flowers so diverse?
1459 Reduction of evolutionary constraints by paralogues of class B floral homeotic genes. Ann.
1460 Bot. **104**: 583–594.

1461 **Moriyama, Y., Ito, F., Takeda, H., Yano, T., Okabe, M., Kuraku, S., Keeley, F.W., and**
1462 **Koshiba-Takeuchi, K.** (2016). Evolution of the fish heart by sub/neofunctionalization of
1463 an elastin gene. Nat. Commun. **7**: 10397.

1464 **Ogburn, R.M. and Edwards, E.J.** (2009). Anatomical variation in Cactaceae and relatives: Trait
1465 lability and evolutionary innovation. Am. J. Bot. **96**: 391–408.

1466 **Ohno, S.** (1970). Evolution by gene duplication (Springer Berlin: Heidelberg).

1467 **Osmond, C.B.** (1978). Crassulacean Acid Metabolism: A Curiosity in Context. Annu. Rev. Plant
1468 Physiol. **29**: 379–414.

1469 **Otto, F.J., Oldiges, H., Göhde, W., and Jain, V.K.** (1981). Flow cytometric measurement of
1470 nuclear DNA content variations as a potential in vivo mutagenicity test. Cytometry **2**: 189–
1471 191.

1472 **Ou, S. et al.** (2019). Benchmarking transposable element annotation methods for creation of a
1473 streamlined, comprehensive pipeline. Genome Biol. **20**: 275.

1474 **Pedro, D.L.F., Amorim, T.S., Varani, A., Guyot, R., Domingues, D.S., and Paschoal, A.R.**
1475 (2021). An Atlas of Plant Transposable Elements. F1000Res. **10**: 1194.

1476 **Philippe, F., Verdu, I., Morère-Le Paven, M.-C., Limami, A.M., and Planchet, E.** (2019).
1477 Involvement of Medicago truncatula glutamate receptor-like channels in nitric oxide
1478 production under short-term water deficit stress. J. Plant Physiol. **236**: 1–6.

1479 **Pierce, S., Winter, K., and Griffiths, H.** (2002). Carbon isotope ratio and the extent of daily
1480 CAM use by Bromeliaceae. New Phytol. **156**: 75–83.

1481 **Popp, M., Janett, H.-P., Lüttge, U., and Medina, E.** (2003). Metabolite gradients and
1482 carbohydrate translocation in rosette leaves of CAM and C3 bromeliads. New Phytol. **157**:
1483 649–656.

1484 **Putnam, N.H. et al.** (2016). Chromosome-scale shotgun assembly using an in vitro method for
1485 long-range linkage. Genome Res. **26**: 342–350.

1486 **Quezada, I.M. and Gianoli, E.** (2011). Crassulacean acid metabolism photosynthesis in
1487 Bromeliaceae: an evolutionary key innovation. Biol. J. Linn. Soc. Lond. **104**: 480–486.

1488 **Ranwez, V., Douzery, E.J.P., Cambon, C., Chantret, N., and Delsuc, F.** (2018). MACSE v2:
1489 Toolkit for the Alignment of Coding Sequences Accounting for Frameshifts and Stop
1490 Codons. Mol. Biol. Evol. **35**: 2582–2584.

1491 **Roach, M.J., Schmidt, S.A., and Borneman, A.R.** (2018). Purge Haplotigs: allelic contig
1492 reassignment for third-gen diploid genome assemblies. BMC Bioinformatics **19**: 460.

1493 **Robinson, M.D., McCarthy, D.J., and Smyth, G.K.** (2009). edgeR: A Bioconductor package for
1494 differential expression analysis of digital gene expression data. Bioinformatics **26**: 139–
1495 140.

1496 **Schubert, M., Lindgreen, S., and Orlando, L.** (2016). AdapterRemoval v2: rapid adapter
1497 trimming, identification, and read merging. BMC Res. Notes **9**: 88.

1498 **Silvera, K., Neubig, K.M., Mark Whitten, W., Williams, N.H., Winter, K., and Cushman,**
1499 **J.C.** (2010). Evolution along the crassulacean acid metabolism continuum. Funct. Plant
1500 Biol. **37**: 995–1010.

1501 **Silvera, K., Santiago, L.S., Cushman, J.C., and Winter, K.** (2009). Crassulacean acid
1502 metabolism and epiphytism linked to adaptive radiations in the Orchidaceae. Plant Physiol.
1503 **149**: 1838–1847.

1504 **Silvera, K., Winter, K., Rodriguez, B.L., Albion, R.L., and Cushman, J.C.** (2014). Multiple
1505 isoforms of phosphoenolpyruvate carboxylase in the Orchidaceae (subtribe Oncidiinae):
1506 implications for the evolution of crassulacean acid metabolism. J. Exp. Bot. **65**: 3623–
1507 3636.

1508 **Simpson, G.G.** (1953). The Major Features of Evolution (Columbia University Press).

1509 **Smit, A.F.A., Hubley, R., and Green, P.** (2013-2015). RepeatMasker Open-4.0.

1510 **Stanke, M., Diekhans, M., Baertsch, R., and Haussler, D.** (2008). Using native and syntenically
1511 mapped cDNA alignments to improve de novo gene finding. Bioinformatics **24**: 637–644.

1512 **Tay, I.Y.Y., Odang, K.B., and Cheung, C.Y.M.** (2021). Metabolic Modeling of the C3-CAM
1513 Continuum Revealed the Establishment of a Starch/Sugar-Malate Cycle in CAM
1514 Evolution. Front. Plant Sci. **11**: 2221.

1515 **Temsch, E.M.** (2010). Genome size in liverworts. Preslia **82**: 63–80.

1516 **Temsch, E.M., Koutecký, P., Urfus, T., Šmarda, P., and Doležel, J.** (2022). Reference standards
1517 for flow cytometric estimation of absolute nuclear DNA content in plants. Cytometry A
1518 **101**: 710–724.

1519 **Töpfer, N., Braam, T., Shameer, S., Ratcliffe, R.G., and Sweetlove, L.J.** (2020). Alternative
1520 Crassulacean Acid Metabolism Modes Provide Environment-Specific Water-Saving
1521 Benefits in a Leaf Metabolic Model. Plant Cell **32**: 3689–3705.

1522 **Tsugawa, H., Cajka, T., Kind, T., Ma, Y., Higgins, B., Ikeda, K., Kanazawa, M.,**

1523 **VanderGheynst, J., Fiehn, O., and Arita, M.** (2015). MS-DIAL: data-independent
1524 MS/MS deconvolution for comprehensive metabolome analysis. Nat. Methods **12**: 523–
1525 526.

1526 **Vera-Estrella, R., Barkla, B.J., Amezcua-Romero, J.C., and Pantoja, O.** (2012). Day/night
1527 regulation of aquaporins during the CAM cycle in Mesembryanthemum crystallinum. Plant
1528 Cell Environ. **35**: 485–501.

1529 **de Vos, J.M., Augustijnen, H., Bätscher, L., and Lucek, K.** (2020). Speciation through
1530 chromosomal fusion and fission in Lepidoptera. Philos. Trans. R. Soc. Lond. B Biol. Sci.
1531 **375**: 20190539.

1532 **Wai, C.M. et al.** (2017). Temporal and spatial transcriptomic and microRNA dynamics of CAM
1533 photosynthesis in pineapple. Plant J. **92**: 19–30.

1534 **Walker, B.J., Abeel, T., Shea, T., Priest, M., Abouelliel, A., Sakthikumar, S., Cuomo, C.A.,**
1535 **Zeng, Q., Wortman, J., Young, S.K., and Earl, A.M.** (2014). Pilon: an integrated tool
1536 for comprehensive microbial variant detection and genome assembly improvement. PLoS
1537 One **9**: e112963.

1538 **Waterhouse, R.M., Seppey, M., Simão, F.A., Manni, M., Ioannidis, P., Klioutchnikov, G.,**
1539 **Kriventseva, E.V., and Zdobnov, E.M.** (2018). BUSCO Applications from Quality
1540 Assessments to Gene Prediction and Phylogenomics. Mol. Biol. Evol. **35**: 543–548.

1541 **Weckwerth, W., Wenzel, K., and Fiehn, O.** (2004). Process for the integrated extraction,
1542 identification and quantification of metabolites, proteins and RNA to reveal their co-
1543 regulation in biochemical networks. Proteomics **4**: 78–83.

1544 **Weiland, M., Mancuso, S., and Baluska, F.** (2015). Signalling via glutamate and GLRs in
1545 Arabidopsis thaliana. Funct. Plant Biol. **43**: 1–25.

1546 **Wickell, D. et al.** (2021). Underwater CAM photosynthesis elucidated by Isoetes genome. Nature
1547 Communications 2021 12:1 **12**: 1–13.

1548 **Winter, K., Garcia, M., Virgo, A., and Smith, J.A.C.** (2021). Low-level CAM photosynthesis
1549 in a succulent-leaved member of the Urticaceae, Pilea peperomioides. Funct. Plant Biol.
1550 **48**: 683–690.

1551 **Winter, K. and Smith, J.A.C.** (2022). CAM photosynthesis: the acid test. New Phytol. **233**: 599–
1552 609.

1553 **Winter, K. and Smith, J.A.C.** (2012). Crassulacean Acid Metabolism: Biochemistry,
1554 Ecophysiology and Evolution (Springer: Berlin, Germany).

1555 **Wong, W.S.W., Yang, Z., Goldman, N., and Nielsen, R.** (2004). Accuracy and power of
1556 statistical methods for detecting adaptive evolution in protein coding sequences and for
1557 identifying positively selected sites. Genetics **168**: 1041–1051.

1558 **Xiao, B., Huang, Y., Tang, N., and Xiong, L.** (2007). Over-expression of a LEA gene in rice

1559 improves drought resistance under the field conditions. Züchter Genet. Breed. Res. **115**:
1560 35–46.

1561 **Yang, X. et al.** (2017). The Kalanchoë genome provides insights into convergent evolution and
1562 building blocks of crassulacean acid metabolism. Nat. Commun. **8**: 1899.

1563 **Yang, Z.** (2007). PAML 4: Phylogenetic Analysis by Maximum Likelihood. Mol. Biol. Evol. **24**:
1564 1586–1591.

1565 **Yardeni, G. et al.** (2021). Taxon-specific or universal? Using target capture to study the
1566 evolutionary history of rapid radiations. Mol. Ecol. Resour.

1567 **Zhang, S., Ghatak, A., and Bazargani, M.** (2023). Cell-type proteomic and metabolomic
1568 resolution of early and late grain filling stages of wheat endosperm. Plant Biotechnology
1569 Journal.

1570 **Zhu, F. and Ming, R.** (2019). Global identification and expression analysis of pineapple
1571 aquaporins revealed their roles in CAM photosynthesis, boron uptake and fruit
1572 domestication. Euphytica **215**: 132.

1573